CHINA CDC WEEKLY

CCDCweekly

中 国 疾 病 预 防 控 制 中 心 周 报

COP28

United Nations Climate Change

The 28th Conference of the Parties (COP28):

Climate action can't wait.

Cover Image: adapted from the United Nations, https://www.un.org/zh/climatechange/cop28.

Announcements

The 28th United Nations Climate Change Conference (COP28) — November 30 to December 12, 2023

Qiyong Liu[#]

The United Nations climate change conferences serve as annual global forums for multilateral discussions on climate change. The COP28 (November 30 to December 12, 2023) bears significant importance in light of record high global temperatures and the widespread impact of extreme weather events. It presents a crucial opportunity to redirect our efforts and accelerate actions toward addressing the climate crisis and the health crisis (1).

At the COP28, there will be an emphasis on climate and health, with a focus on adapting to climate change and implementing mitigation strategies to protect human health. China must prioritize climate action in response to the growing health risks associated with climate change. To support vulnerable populations, such as individuals with cardiorespiratory diseases, the elderly, and pregnant women, in coping with the consequences of climate change, the health section of China's National Climate Change Adaptation Strategy 2035 has proposed various measures. Additionally, it is essential to conduct assessments in China to evaluate the health effects stemming from climate policies, alongside emission reductions to achieve climate targets (2).

REFERENCES

1. United Nations. COP28: climate action can't wait. 2023. https://www.un.org/en/climatechange/cop28. [2023-12-2].
2. Woodward A, Baumgartner J, Ebi KL, Gao JH, Kinney PL, Liu QY. Population health impacts of China's climate change policies. Environ Res 2019;175:178 – 85. http://dx.doi.org/10.1016/j.envres.2019.05.020.

Preplanned Studies

Disparities of Heatwave-Related Preterm Birth in Climate Types — China, 2012–2019

Yafei Guo[1,2,&]; Yanxia Xie[3,4,&]; Xiaohui Wei[5,1]; Chenran Guo[5,1]; Peiran Chen[3,4]; Yanping Wang[3,4]; Yi Mu[3,4]; Xiaoming Shi[6]; Jun Zhu[3,4]; Juan Liang[3,4,#]; Qiyong Liu[1,5,#]

Summary

What is already known about this topic?

An association between prenatal heatwave exposure and the risk of preterm birth was found. However, the disparities in heatwave-related preterm birth across different climate types have not been examined.

What is added by this report?

This nationwide case-crossover study investigated the association between heatwave exposure and preterm birth across different Köppen-Geiger climate types. Among pregnant women residing in the arid-desert-cold climate type, exposure to compound heatwaves was found to be associated with a significantly higher risk of preterm birth {adjusted odds ratios (AORs) ranged from 1.55 [95% confidence interval (CI): 1.21–1.97] to 2.11 (95% CI: 1.35–3.31)}. In contrast, among pregnant women residing in the tropical monsoonal climate type, exposure to daytime-only heatwaves was associated with an increased risk of preterm birth [AORs ranged from 1.25 (95% CI: 1.03–1.51) to 1.37 (95% CI: 1.05–1.77)].

What are the implications for public health practice?

Specific interventions should be implemented in China to mitigate the risk of preterm birth related to heatwaves, particularly for pregnant women residing in arid-desert-cold and tropical monsoonal climates.

Recent systematic reviews have identified a need for studies investigating the association between high temperatures and preterm birth (PTB) across different climate types (1–2). Previous research has suggested that the association between extreme heat and PTB may vary depending on the climate (3–4), and there is also variability in the definition of heatwaves used in different studies (5). Furthermore, recent studies have revealed differences in the dominant subtypes of heat

episodes across regions in China (6). To enhance our understanding of this topic, we conducted a large, nationally representative case-crossover study using data from China's national maternal surveillance system encompassing 5,446,088 participants from 2012 to 2019. Our study aimed to examine the risk of PTB associated with 18 different definitions of heatwaves in various climate types according to the Köppen-Geiger classification. Our findings indicate that pregnant women in the arid-desert-cold climate type faced a higher risk of PTB when exposed to compound heatwaves, while those in the tropical monsoonal climate type experienced an increased risk with daytime-only heatwaves. These results provide valuable evidence for the development of targeted strategies for heat-PTB prevention in China, taking into account the disparities in heatwave-related PTB among different climate types.

We obtained data on singleton live births from China's National Maternal Near Miss Surveillance System (NMNMSS) for the period between January 1, 2012, and December 31, 2019, as data for 2020–2022 were not available during the study period. The data included information from 438 health facilities in 325 counties or districts across China. We applied four exclusion criteria and extracted a final analytic sample of 5,446,088 births in the warm season (April to October), as described elsewhere (7). The NMNMSS was approved by the Ethics Committee of West China Second University Hospital, Sichuan University, China (Protocol ID: 2012008), and adhered to the principles of the Declaration of Helsinki. The ethical approval (Protocol ID: 2012008) also authorized the use of NMNMSS data for subsequent studies, including the current study, on maternal health.

We defined PTB as births occurring before 37 completed weeks of gestation. To assign climate types for eligible birth records, we used the addresses of the delivery health facilities for each pregnant woman, as residential addresses were not available in the NMNMSS. Climate types were classified based on the updated Köppen-Geiger climate classification. We obtained climate classification data from the 1 km global Köppen-Geiger raster product for the time period 1981–2010 from Climatologies at high resolution for the earth's land surface areas (CHELSA) (8). Daily maximum temperature (Tmax), minimum temperature (Tmin), relative humidity, and fine particulate matter levels with an aerodynamic diameter less than or equal to 2.5 ($PM_{2.5}$) were extracted. To assign exposure, we calculated the mean grid from a zone with a 25-km radius around each pregnant woman's delivery address. Detailed information on the calculation method can be found elsewhere (7). We defined 18 types of heatwaves, categorized into three distinct types: daytime-only (Tmax exceeds thresholds only), nighttime-only (Tmin exceeds thresholds only), and compound (both Tmax and Tmin exceed thresholds). We used six indexes, namely 75th-D2, 75th-D3, 75th-D4, 90th-D2, 90th-D3, and 90th-D4, which represent periods of equal to or more than two, three, or four consecutive days above the daily temperature thresholds at the 75th or 90th percentiles. (Supplementary Material, available in https://weekly.chinacdc.cn/).

In this multisite study, a space-time-stratified case-crossover design was used to examine the relationship between heatwave events and PTB. This design allowed each participant to serve as her own control and compared exposure on case days to control days (7). Time-invariant individual level confounders, as well as long-term and seasonal trends, were controlled for in the design. Conditional logistic regression models were employed to assess the association between heatwave events and PTB. The models were adjusted for the moving average of relative humidity and $PM_{2.5}$ in the last gestational week (lag06), calculated across the time window, using a natural cubic spline with 3 df. The analysis explored the variation in climate zones using an interaction term between the heatwave exposure variable and the category variable for climate types. The reference group for this analysis was the tropical monsoonal (Am) climate type. The significance of the interaction term was tested using a two-sided P-value of <0.05. Each of the three types of heatwave definitions and six indexes were modeled individually. Additionally, the lag effects of the final week prior to delivery were investigated. We estimated the odds ratio employing the maximized model goodness of fit in the seven lag days (lag0, lag1, lag2, lag3, lag4, lag5, lag6) for each heatwave definition (9).

All analyses were performed using R software (version 4.1.1, R Project for Statistical Computing, Vienna, Austria). The "survival" package (version 3.2.11) and the "splines" package (version 4.1.1) were employed for conducting the conditional logistic regression analysis.

In the final analytic sample, which included a total of 5,446,088 participants, we observed coverage of 10 different Köppen-Geiger climate types. These types encompassed two tropical [Tropical-monsoon (Am)

and Tropical-savannah (Aw)], two arid [Arid-steppe-cold (BSk) and Arid-desert-cold (BWk)], three temperate [Temperate-fully humid-hot summer (Cfa), Temperate-dry winter-hot summer (Cwa), and Temperate-dry winter-warm summer (Cwb)], and three cold [Cold-fully humid-hot summer (Dfa), Cold-dry winter-hot summer (Dwa), and Cold-dry winter-warm summer (Dwb)] climate types (Supplementary Table S1, available in https://weekly.chinacdc.cn/). The majority of participants (68.93%) resided in temperate climate types (Table 1). The rate of PTB did not vary significantly among tropical, arid, temperate, and cold climate types (Table 1). However, pregnant women living in tropical climate types experienced higher exposure to compound and nighttime heat waves during the study period. Conversely, women in arid climate types experienced less exposure to compound heat waves (Table 2).

Pregnant women in arid BWk climate type endure a higher risk of PTB {adjusted odds ratio (AOR) range, 1.55 [95% confidence interval (CI): 1.21–1.97] to 2.11 (95% CI: 1.35–3.31)} than tropical Am climate type during exposure to compound heat waves in the 90th-D3 and 90th-D4 indexes (Figure 1). When exposed to daytime-only heat waves, pregnant women in tropical Am climate type also face a higher risk of

PTB [AOR range, 1.25 (95% CI: 1.03–1.51) to 1.37 (95% CI: 1.05–1.77)] than other climate types in the 75th-D2, 75th-D3, 90th-D3, and 90th-D4 indexes. The risk of PTB for pregnant women in arid BWk climate type is associated with exposure to nighttime-only heat waves in the 90th-D4 index [AOR, 1.23 (95% CI: 1.00–1.51)], with no significant difference compared with tropical Am pregnant women.

DISCUSSION

In our nationwide study examining the relationship between heat waves and PTB across ten different climate types as classified by the Köppen-Geiger system, we observed varying associations. Specifically, among pregnant women exposed to daytime-only heat waves, those residing in the tropical Am climate type faced an elevated risk of PTB [AOR range, 1.25 (95% CI: 1.03–1.51) to 1.37 (95% CI: 1.05–1.77)]. Additionally, for pregnant women exposed to compound heat waves, those living in the arid BWk climate type experienced a higher risk of PTB [AOR range, 1.55 (95% CI: 1.21–1.97) to 2.11 (95% CI: 1.35–3.31)].

Previous studies have examined the association between extreme heat exposure during pregnancy and

TABLE 1. Climate zonal characteristics of participants.

Characteristic		Participants, n	Preterm births, n (%)[†]	Sampled sites (health facilities), n	Sampled counties, n[§]
Total		5,446,088	310,384 (5.70)	438	325
Climate type and descriptions*					
A	Tropical	134,653	7,606 (5.65)	11	8
Am	Tropical-monsoon	57,221	2,685 (4.69)	6	4
Aw	Tropical-savannah	77,432	4,921 (6.36)	5	4
B	Arid	777,351	45,465 (5.85)	82	63
BSk	Arid-steppe-cold	640,730	38,082 (5.94)	66	52
BWk	Arid-desert-cold	136,621	7,383 (5.40)	16	11
C	Temperate	3,754,084	216,811 (5.78)	267	191
Cfa	Temperate-fully humid-hot summer	2,147,735	129,056 (6.01)	145	106
Cwa	Temperate-dry winter-hot summer	1,455,039	78,931 (5.42)	108	77
Cwb	Temperate-dry winter-warm summer	151,310	8,824 (5.83)	14	8
D	Cold	780,000	40,502 (5.19)	78	65
Dfa	Cold-fully humid-hot summer	42,162	2,633 (6.24)	4	2
Dwa	Cold-dry winter-hot summer	648,889	35,134 (5.41)	58	48
Dwb	Cold-dry winter-warm summer	88,949	2,735 (3.07)	16	15

* Climate types and descriptions followed the updated Köppen-Geiger climate classification.
† Percentages are calculated from participants' number of all singleton births during the warm season (April to October) in China in each category of climate types.
§ Two sampled counties covered both arid BSk and cold Dwa climate types.

TABLE 2. Summary of climate zonal heat waves in the warm season during 2012–2019.

Heatwave definitions*		Köppen-Geiger Climate Types											
		Tropical			Arid			Temperate			Cold		
Types	Indexes	Cut off Tmax[†] (°C)	Cut off Tmin[†] (°C)	Heatwave days/site/year[§] (%)	Cut off Tmax[†] (°C)	Cut off Tmin[†] (°C)	Heatwave days/site/year[§] (%)	Cut off Tmax[†] (°C)	Cut off Tmin[†] (°C)	Heatwave days/site/year[§] (%)	Cut off Tmax[†] (°C)	Cut off Tmin[†] (°C)	Heatwave days/site/year[§] (%)
Daytime-only heat wave	75th-D2	32.98	17.95	18.50 (8.64)	26.25	18.13	26.40 (12.34)	29.54	17.96	22.53 (10.53)	25.59	17.47	22.57 (10.55)
	75th-D3	32.98	17.95	11.92 (5.57)	26.25	18.13	15.84 (7.40)	29.54	17.96	14.07 (6.57)	25.59	17.47	12.75 (5.96)
	75th-D4	32.98	17.95	8.48 (3.96)	26.25	18.13	9.17 (4.28)	29.54	17.96	9.16 (4.28)	25.59	17.47	7.63 (3.57)
	90th-D2	33.88	19.50	13.34 (6.23)	28.24	19.57	13.23 (6.18)	31.24	19.35	12.85 (6.01)	27.64	18.84	11.35 (5.30)
	90th-D3	33.88	19.50	8.20 (3.83)	28.24	19.57	6.87 (3.21)	31.24	19.35	7.16 (3.35)	27.64	18.84	5.65 (2.64)
	90th-D4	33.88	19.50	5.58 (2.61)	28.24	19.57	3.64 (1.70)	31.24	19.35	4.03 (1.88)	27.64	18.84	2.79 (1.30)
Nighttime-only heat wave	75th-D2	32.98	17.95	36.16 (16.90)	26.25	18.13	26.55 (12.41)	29.54	17.96	21.09 (9.85)	25.59	17.47	22.38 (10.46)
	75th-D3	32.98	17.95	23.99 (11.21)	26.25	18.13	14.93 (6.98)	29.54	17.96	11.88 (5.55)	25.59	17.47	11.85 (5.54)
	75th-D4	32.98	17.95	16.74 (7.82)	26.25	18.13	8.95 (4.18)	29.54	17.96	6.66 (3.11)	25.59	17.47	6.14 (2.87)
	90th-D2	33.88	19.50	23.35 (10.91)	28.24	19.57	12.67 (5.92)	31.24	19.35	11.35 (5.30)	27.64	18.84	10.21 (4.77)
	90th-D3	33.88	19.50	14.65 (6.84)	28.24	19.57	6.55 (3.06)	31.24	19.35	6.03 (2.82)	27.64	18.84	4.76 (2.23)
	90th-D4	33.88	19.50	8.78 (4.10)	28.24	19.57	3.28 (1.53)	31.24	19.35	3.08 (1.44)	27.64	18.84	2.17 (1.02)
Compound heat wave	75th-D2	32.98	17.95	49.45 (23.11)	26.25	18.13	20.25 (9.46)	29.54	17.96	30.77 (14.38)	25.59	17.47	22.36 (10.45)
	75th-D3	32.98	17.95	41.01 (19.16)	26.25	18.13	14.07 (6.57)	29.54	17.96	23.76 (11.10)	25.59	17.47	15.31 (7.15)
	75th-D4	32.98	17.95	35.34 (16.51)	26.25	18.13	9.62 (4.49)	29.54	17.96	17.44 (8.15)	25.59	17.47	9.96 (4.65)
	90th-D2	33.88	19.50	19.44 (9.09)	28.24	19.57	4.39 (2.05)	31.24	19.35	9.66 (4.52)	27.64	18.84	5.67 (2.65)
	90th-D3	33.88	19.50	13.94 (6.52)	28.24	19.57	2.33 (1.09)	31.24	19.35	6.47 (3.02)	27.64	18.84	2.88 (1.34)
	90th-D4	33.88	19.50	11.42 (5.34)	28.24	19.57	1.31 (0.61)	31.24	19.35	4.25 (1.98)	27.64	18.84	1.59 (0.74)

* 18 definitions of heat waves with three types, daytime-only (only daily maximum temperature exceeds thresholds), nighttime-only (only daily minimum temperature exceeds thresholds), and compound (both daily maximum and minimum temperature exceeds thresholds) heat waves, and six indexes, 75th-D2, 75th-D3, 75th-D4, 90th-D2, 90th-D3, and 90th-D4 (periods equal to or more than two, three, or four consecutive days above the daily thresholds of temperature as 75th or 90th percentiles).
[†] Tmax, daily maximum temperature; Tmin, daily minimum temperature.
[§] Percentages are calculated using 214 days in the warm season (April to October) as the denominator.

A Daytime-only heat wave **B** Nighttime-only heat wave **C** Compound heat wave

Heat wave duration and climate type	A AOR (95% CI)	A P value	B AOR (95% CI)	B P value	C AOR (95% CI)	C P value
Days exceeding 75th percentile						
2d						
Am	1.27 (1.08, 1.49)	[Ref]	0.86 (0.76, 0.97)	[Ref]	1.10 (0.99, 1.22)	[Ref]
Aw	1.04 (0.92, 1.17)	0.07	0.96 (0.88, 1.04)	0.23	1.05 (0.97, 1.14)	0.64
BSk	0.98 (0.95, 1.02)	0.003*	1.01 (0.98, 1.05)	0.02*	1.05 (1.01, 1.09)	0.43
BWk	0.97 (0.89, 1.05)	0.002*	1.05 (0.96, 1.15)	0.02*	0.99 (0.91, 1.09)	0.17
Cfa	0.99 (0.97, 1.01)	0.003*	1.02 (0.99, 1.04)	0.009*	1.00 (0.98, 1.02)	0.10
Cwa	1.02 (0.99, 1.05)	0.008*	1.00 (0.97, 1.03)	0.02*	1.02 (1.00, 1.05)	0.20
Cwb	1.01 (0.95, 1.09)	0.009*	1.02 (0.95, 1.11)	0.02*	1.05 (0.97, 1.13)	0.37
Dfa	1.26 (1.08, 1.48)	0.93	0.76 (0.62, 0.94)	0.32	1.07 (0.95, 1.22)	0.84
Dwa	0.99 (0.95, 1.03)	0.003*	0.96 (0.92, 1.00)	0.10	1.01 (0.97, 1.05)	0.17
Dwb	0.95 (0.83, 1.09)	0.005*	0.99 (0.86, 1.14)	0.11	1.01 (0.86, 1.19)	0.31
3d						
Am	1.25 (1.03, 1.51)	[Ref]	0.86 (0.75, 1.00)	[Ref]	1.10 (0.98, 1.24)	[Ref]
Aw	1.00 (0.87, 1.16)	0.09	0.83 (0.75, 0.93)	0.70	1.03 (0.95, 1.13)	0.51
BSk	0.97 (0.92, 1.01)	0.01*	1.00 (0.96, 1.05)	0.06	1.04 (0.99, 1.09)	0.33
BWk	0.94 (0.85, 1.04)	0.008*	0.95 (0.84, 1.07)	0.37	1.02 (0.93, 1.13)	0.39
Cfa	1.01 (0.98, 1.04)	0.03*	0.99 (0.96, 1.02)	0.07	1.01 (0.99, 1.03)	0.15
Cwa	1.03 (1.00, 1.07)	0.04*	0.98 (0.95, 1.02)	0.09	1.01 (0.99, 1.04)	0.15
Cwb	1.03 (0.95, 1.11)	0.05*	1.08 (0.98, 1.19)	0.01*	1.08 (0.99, 1.18)	0.67
Dfa	1.32 (1.02, 1.71)	0.78	0.91 (0.67, 1.23)	0.83	1.16 (1.01, 1.33)	0.52
Dwa	0.97 (0.91, 1.02)	0.01*	0.98 (0.92, 1.04)	0.13	0.99 (0.95, 1.04)	0.12
Dwb	0.92 (0.76, 1.11)	0.02*	0.92 (0.77, 1.11)	0.44	1.06 (0.87, 1.29)	0.59
4d						
Am	1.13 (0.90, 1.42)	[Ref]	0.90 (0.77, 1.07)	[Ref]	1.11 (0.98, 1.26)	[Ref]
Aw	0.92 (0.78, 1.08)	0.16	0.84 (0.74, 0.95)	0.40	1.11 (1.01, 1.21)	0.89
BSk	0.99 (0.93, 1.05)	0.24	1.00 (0.95, 1.06)	0.25	1.03 (0.98, 1.09)	0.33
BWk	1.08 (0.94, 1.24)	0.63	0.93 (0.80, 1.09)	0.87	1.02 (0.92, 1.14)	0.38
Cfa	1.05 (1.01, 1.08)	0.46	1.00 (0.96, 1.04)	0.25	1.01 (0.99, 1.03)	0.15
Cwa	1.02 (0.97, 1.06)	0.32	0.96 (0.92, 1.00)	0.51	1.01 (0.98, 1.04)	0.14
Cwb	1.10 (1.00, 1.21)	0.70	1.10 (0.96, 1.25)	0.07	1.08 (0.97, 1.20)	0.67
Dfa	1.28 (0.96, 1.71)	0.48	0.74 (0.45, 1.23)	0.45	1.11 (0.95, 1.31)	0.94
Dwa	1.00 (0.93, 1.07)	0.29	0.95 (0.86, 1.05)	0.62	0.99 (0.94, 1.05)	0.15
Dwb	0.94 (0.74, 1.19)	0.23	0.93 (0.73, 1.18)	0.71	1.10 (0.84, 1.44)	0.88

0.55 0.85 1.15 1.45 1.75 AOR (95% CI) (panels A and B) 0.55 0.85 1.15 1.45 1.75 AOR (95% CI) (panel C)

Heat wave duration and climate type	A AOR (95% CI)	A P value	B AOR (95% CI)	B P value	C AOR (95% CI)	C P value
Days exceeding 90th percentile						
2d						
Am	1.07 (0.90, 1.28)	[Ref]	1.10 (0.96, 1.27)	[Ref]	1.17 (1.01, 1.35)	[Ref]
Aw	0.91 (0.79, 1.05)	0.18	0.89 (0.80, 0.98)	0.01*	1.10 (0.98, 1.23)	0.64
BSk	1.00 (0.95, 1.05)	0.46	1.03 (0.98, 1.09)	0.41	0.98 (0.91, 1.07)	0.05
BWk	1.04 (0.93, 1.15)	0.70	1.02 (0.91, 1.14)	0.39	0.93 (0.76, 1.13)	0.07
Cfa	1.05 (1.02, 1.08)	0.83	0.99 (0.96, 1.02)	0.14	1.00 (0.97, 1.03)	0.05
Cwa	1.03 (1.00, 1.07)	0.67	1.01 (0.98, 1.05)	0.26	1.02 (0.98, 1.06)	0.08
Cwb	1.02 (0.94, 1.10)	0.57	0.99 (0.89, 1.11)	0.25	1.07 (0.95, 1.22)	0.37
Dfa	1.00 (0.81, 1.23)	0.58	1.09 (0.84, 1.41)	0.84	1.08 (0.86, 1.35)	0.59
Dwa	1.00 (0.95, 1.05)	0.47	1.00 (0.94, 1.06)	0.20	1.04 (0.97, 1.12)	0.21
Dwb	1.03 (0.85, 1.25)	0.67	0.95 (0.77, 1.17)	0.29	1.10 (0.79, 1.53)	0.62
3d						
Am	1.34 (1.07, 1.68)	[Ref]	1.00 (0.83, 1.20)	[Ref]	1.06 (0.90, 1.26)	[Ref]
Aw	1.01 (0.86, 1.18)	0.04*	0.89 (0.79, 1.01)	0.30	1.10 (0.97, 1.25)	0.66
BSk	0.96 (0.90, 1.03)	0.005*	0.98 (0.91, 1.05)	0.84	1.00 (0.89, 1.11)	0.49
BWk	1.03 (0.90, 1.18)	0.04*	1.00 (0.86, 1.17)	0.98	1.55 (1.21, 1.97)	0.02*
Cfa	1.05 (1.01, 1.10)	0.03*	1.01 (0.97, 1.05)	0.87	1.00 (0.96, 1.04)	0.43
Cwa	1.04 (1.00, 1.09)	0.02*	1.03 (0.98, 1.08)	0.74	0.98 (0.94, 1.03)	0.33
Cwb	1.15 (1.04, 1.27)	0.17	1.05 (0.90, 1.23)	0.67	0.92 (0.78, 1.09)	0.22
Dfa	0.81 (0.58, 1.13)	0.01*	0.79 (0.47, 1.32)	0.35	1.00 (0.74, 1.36)	0.77
Dwa	0.98 (0.90, 1.05)	0.008*	0.98 (0.89, 1.08)	0.91	1.05 (0.94, 1.17)	0.96
Dwb	0.95 (0.70, 1.28)	0.05*	1.20 (0.91, 1.59)	0.23	0.82 (0.47, 1.44)	0.31
4d						
Am	1.37 (1.05, 1.77)	[Ref]	0.92 (0.73, 1.17)	[Ref]	1.05 (0.88, 1.26)	[Ref]
Aw	0.95 (0.78, 1.15)	0.03*	0.93 (0.79, 1.10)	0.97	1.13 (0.98, 1.30)	0.51
BSk	0.97 (0.89, 1.05)	0.01*	0.92 (0.84, 1.02)	>0.99	0.99 (0.85, 1.14)	0.54
BWk	0.96 (0.80, 1.14)	0.02*	1.23 (1.00, 1.51)	0.10	2.11 (1.35, 3.31)	0.007*
Cfa	1.07 (1.01, 1.13)	0.06	0.97 (0.92, 1.02)	0.71	0.99 (0.94, 1.03)	0.44
Cwa	1.02 (0.96, 1.08)	0.02*	1.01 (0.94, 1.07)	0.50	1.00 (0.94, 1.05)	0.51
Cwb	1.13 (0.99, 1.28)	0.15	1.03 (0.82, 1.28)	0.51	0.97 (0.78, 1.21)	0.56
Dfa	1.24 (0.70, 2.17)	0.79	0.28 (0.07, 1.21)	0.11	0.78 (0.49, 1.24)	0.25
Dwa	0.99 (0.90, 1.09)	0.02*	0.90 (0.77, 1.05)	0.85	1.00 (0.85, 1.17)	0.69
Dwb	0.99 (0.60, 1.62)	0.24	1.09 (0.75, 1.57)	0.43	0.89 (0.46, 1.71)	0.52

0.55 0.85 1.15 1.45 1.75 AOR (95% CI) (panels A and B) 0.35 1.10 1.85 2.60 3.35 AOR (95% CI) (panel C)
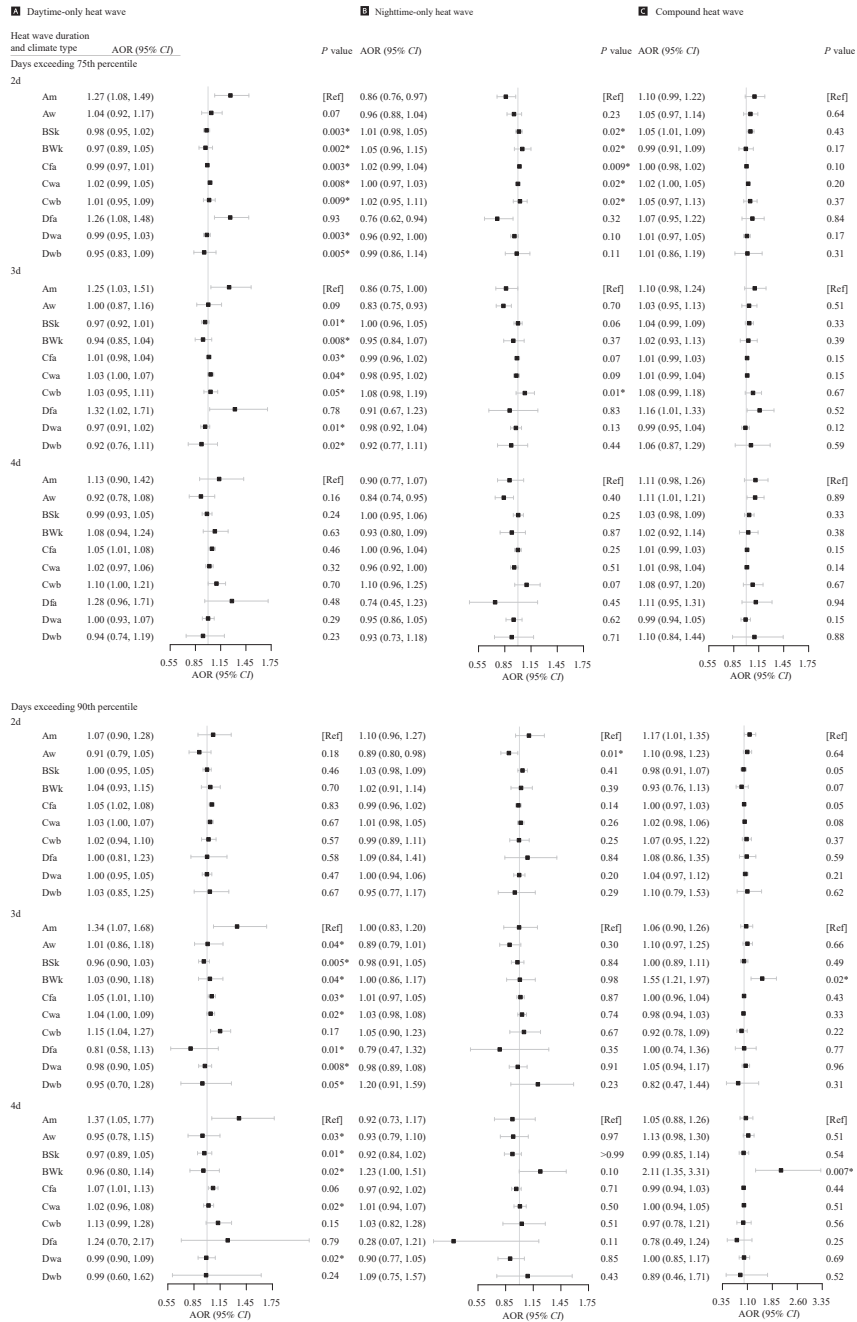
FIGURE 1. AORs of preterm birth associated with heat waves during the last week before delivery among climate types.

Note: 18 definitions of heat waves with three types, daytime-only (only daily maximum temperature exceeds thresholds), nighttime-only (only daily minimum temperature exceeds thresholds), and compound (both daily maximum and minimum temperature exceeds thresholds) heat waves, and six indexes, 75th-D2, 75th-D3, 75th-D4, 90th-D2, 90th-D3, and 90th-D4 (periods equal to or more than two, three, or four consecutive days above the daily thresholds of temperature as 75th or 90th percentiles). Climate types and descriptions followed the updated Köppen-Geiger climate classification. All models adjusted moving average of relative humidity and $PM_{2.5}$ in the last gestational week (lag06), calculated across the time window, using a natural cubic spline with 3 *df*. We examined the climate zonal variation with an interaction term of heatwave exposure variable and climate types' category variable.

Abbreviation: Ref=reference; AOR=adjusted odds ratios; *CI*=confidence interval; Am=Tropical-monsoon; Aw=Tropical-savannah; BSk=Arid-steppe-cold; BWk=Arid-desert-cold; Cfa=Temperate-fully humid-hot summer; Cwa=Temperate-dry winter-hot summer; Cwb=Temperate-dry winter-warm summer; Dfa=Cold-fully humid-hot summer; Dwa=Cold-dry winter-hot summer; Dwb=Cold-dry winter-warm summer.

* Statistically significant.

PTB. These studies exploring associations in the last week before delivery have observed stronger associations in hot-dry/mixed-dry climate zones in the US, with a relative risk of 1.057 (95% *CI*: 1.030–1.083), and in comparative hot areas of China, with an AOR of 1.069 (95% *CI*: 1.010–1.132) (*3,10*). Another study conducted in China found AORs of 2.48 (95% *CI*: 2.37–2.59), 1.62 (95% *CI*: 1.36–1.93), and 1.39 (95% *CI*: 1.33–1.46) for PTB in temperate, tropical, and subtropical zones (*4*), respectively, when exposed to extreme heat throughout the entire pregnancy. Studies mentioned above reported climatic zonal disparities; meanwhile, the AOR of PTB was higher with extreme heat exposure during the entire pregnancy than in the last week before delivery. In comparison to the risk of PTB associated with exposure to heat waves nationwide in China, AORs ranging from 1.02 (95% *CI*: 1.00–1.03) to 1.04 (95% *CI*: 1.01–1.07) for compound heat waves and AORs ranging from 1.03 (95% *CI*: 1.01–1.05) to 1.04 (95% *CI*: 1.01–1.08) for daytime-only heat waves (*7*), our findings provide further evidence of higher associations in specific climate types compared to nationwide estimates.

The association between acute prenatal exposure and PTB is still unclear. Heat-induced PTB can occur due to heat-related dehydration, impaired body temperature regulation, and cardiovascular changes (*11–12*). Differences in the impact of heat on health across geographic regions may be explained by physiological adaptations and adaptive capacities at the individual and community levels, including behavioral, infrastructure, and technological adaptations (*3,13–14*). Our research suggests that lower levels of physiological, behavioral, and technological adaptations in arid climates and during daytime-only heat waves in tropical regions may contribute to the observed findings. Further investigation into the climatic variations of heat-induced PTB could shed light on the underlying mechanisms and inform the development of adaptation services to reduce risks for pregnant women exposed to extreme temperatures.

Our study has several strengths. First, we used finer domains to determine localized heat extremes by utilizing the 25-km radius surrounding each health facility. This allowed us to accurately assess temperature distribution and percentiles. Additionally, we incorporated considerations for human climate adaptation in various climate types by utilizing the temperature distribution from the recent climate state period (1981–2010) as a reference for defining threshold values in each domain. Second, we conducted an analysis of the disparities in heat wave-related preterm births across different climate types. We examined 18 different definitions of heat waves and utilized a comprehensive national sampling database that covered ten diverse climate types. Our findings contribute to the global heat-PTB studies using unified climate classification.

The study has certain limitations that should be acknowledged. First, the study only obtained the delivery hospital addresses of pregnant women from the NMNMSS database. The climate type for each pregnant woman was determined based on the addresses of the delivery health facilities. Although efforts were made to reduce misclassification by calculating the mean grid from a 25-km radius around each address, there may still be potential exposure misclassification. Second, this study is exploratory in nature, specifically investigating the associations between heat waves and PTB in different climate types. Further research is needed to validate these findings.

In conclusion, this study conducted at a national level found that pregnant women residing in arid BWk climate types were at a higher risk of PTB when exposed to compound heat waves during the final week before delivery. Similarly, in tropical regions with an Am climate type, exposure to daytime-only heat waves was associated with an increased risk of PTB. These findings underscore the need for the implementation of heat-PTB prevention strategies that take into account the climate disparities between regions.

Corresponding authors: Qiyong Liu, liuqiyong@icdc.cn; Juan Liang, liangjuan@scu.edu.cn.

1 National Key Laboratory of Intelligent Tracking and Forecasting for Infectious Diseases, National Institute for Communicable Disease Control and Prevention, Chinese Center for Disease Control and Prevention, Beijing, China; 2 Chinese Center for Disease Control and Prevention Key Laboratory of Environment and Population Health, National Institute of Environmental Health, Chinese Center for Disease Control and Prevention, Beijing, China; 3 National Office for Maternal and Child Health Surveillance of China, West China Second University Hospital, Sichuan University, Chengdu City, Sichuan Province, China; 4 Key Laboratory of Birth Defects and Related Diseases of Women and Children (Sichuan University), Ministry of Education, Chengdu City, Sichuan Province, China; 5 School of Public Health, Nanjing Medical University, Nanjing City, Jiangsu Province, China; 6 Chinese Center for Disease Control and Prevention, Beijing, China.
& Joint first authors.

REFERENCES

1. Chersich MF, Pham MD, Areal A, Haghighi MM, Manyuchi A, Swift CP, et al. Associations between high temperatures in pregnancy and risk of preterm birth, low birth weight, and stillbirths: systematic review and meta-analysis. BMJ 2020;371:m3811. http://dx.doi.org/10.1136/bmj.m3811.
2. Zhang YQ, Yu CH, Wang L. Temperature exposure during pregnancy and birth outcomes: an updated systematic review of epidemiological evidence. Environ Pollut 2017;225:700 – 12. http://dx.doi.org/10.1016/j.envpol.2017.02.066.
3. Sun SZ, Weinberger KR, Spangler KR, Eliot MN, Braun JM, Wellenius GA. Ambient temperature and preterm birth: a retrospective study of 32 million US singleton births. Environ Int 2019;126:7 – 13. http://dx.doi.org/10.1016/j.envint.2019.02.023.
4. Wang YY, Li Q, Guo YM, Zhou H, Wang QM, Shen HP, et al. Ambient temperature and the risk of preterm birth: a national birth cohort study in the mainland China. Environ Int 2020;142:105851. http://dx.doi.org/10.1016/j.envint.2020.105851.
5. Kent ST, McClure LA, Zaitchik BF, Smith TT, Gohlke JM. Heat waves and health outcomes in Alabama (USA): the importance of heat wave definition. Environ Health Perspect 2014;122(2):151 – 8. http://dx.doi.org/10.1289/ehp.1307262.
6. Chen Y, Zhai PM. Revisiting summertime hot extremes in China during 1961-2015: overlooked compound extremes and significant changes. Geophys Res Lett 2017;44(10):5096 – 103. http://dx.doi.org/10.1002/2016GL072281.
7. Guo YF, Chen PR, Xie YX, Wang YP, Mu Y, Zhou RB, et al. Association of daytime-only, nighttime-only, and compound heat waves with preterm birth by urban-rural area and regional socioeconomic status in China. JAMA Netw Open 2023;6(8):e2326987. http://dx.doi.org/10.1001/jamanetworkopen.2023.26987.
8. Climatologies at high resolution for the earth's land surface areas. 1 km global Köppen–Geiger climate classification for present and future. https://chelsa-climate.org/1-km-global-koppen-geiger-climate-classification-for-present-and-future/. [2021-11-18].
9. Richardson DB, Cole SR, Chu HT, Langholz B. Lagging exposure information in cumulative exposure-response analyses. Am J Epidemiol 2011;174(12):1416 – 22. http://dx.doi.org/10.1093/aje/kwr260.
10. Guo TJ, Wang YY, Zhang HG, Zhang Y, Zhao J, Wang Y, et al. The association between ambient temperature and the risk of preterm birth in China. Sci Total Environ 2018;613-614:439 – 46. http://dx.doi.org/10.1016/j.scitotenv.2017.09.104.
11. Bouchama A, Abuyassin B, Lehe C, Laitano O, Jay O, O'Connor FG, et al. Classic and exertional heatstroke. Nat Rev Dis Primers 2022;8(1):8. http://dx.doi.org/10.1038/s41572-021-00334-6.
12. Ebi KL, Capon A, Berry P, Broderick C, de Dear R, Havenith G, et al. Hot weather and heat extremes: health risks. Lancet 2021;398(10301):698 – 708. http://dx.doi.org/10.1016/S0140-6736(21)01208-3.
13. Basagaña X, Michael Y, Lensky IM, Rubin L, Grotto I, Vadislavsky E, et al. Low and high ambient temperatures during pregnancy and birth weight among 624,940 singleton term births in Israel (2010–2014): an investigation of potential windows of susceptibility. Environ Health Perspect 2021;129(10):107001. http://dx.doi.org/10.1289/EHP8117.
14. Hondula DM, Balling RC, Vanos JK, Georgescu M. Rising temperatures, human health, and the role of adaptation. Curr Clim Change Rep 2015;1(3):144 – 54. http://dx.doi.org/10.1007/s40641-015-0016-4.

SUPPLEMENTARY MATERIAL

Definition of Heat Waves

We used a three-step process to calculate daily binary variables indicating heatwave day of 18 definitions (three types in six indexes) of heat waves within each health facility's 25 km radius domain during the study period 2012–2019. Firstly, we collected daily Tmax and Tmin for the study period from 1981–2010 and 2012–2019. Second, we calculated daily thresholds, either the 75th or 90th percentile of Tmax or Tmin, within each health facility's 25 km radius domain, using the reference period of 1981–2010. Third, we identified daily indicators for 18 different heatwave definitions for each domain during the study period from 2012–2019.

Daily thresholds were determined using a reference period of 1981–2010. To calculate the thresholds, we considered a window of seven days before and seven days after the target day, resulting in a set of 15 temperature values for each day in each year of the reference period. This generated a total of 450 temperature values, which were used as the reference windows for each day. Percentiles were then calculated for each set of 450 values to establish the daily thresholds.

$$TX_d = \bigcup_{y=1981}^{2010} \bigcup_{i=d-7}^{d+7} Tmax_{y,i}$$

$$TN_d = \bigcup_{y=1981}^{2010} \bigcup_{i=d-7}^{d+7} Tmin_{y,i}$$

For a given day d in a grid cell, the threshold, TX_d, and TN_d are defined as the 75th, or 90th percentile of daily maximum or minimum temperature, centered on a 15-day window (seven days prior and seven days later to a specific day) in the reference period 1981–2010, which has 15 multiply 30 equals to 450 samples.

Where $\bigcup$ denotes the union of 450 sample sets for the given day d;

$Tmax_{y,i}$ is the daily Tmax of the day i in the year y;

$Tmin_{y,i}$ is the daily Tmin of the day i in the year y.

SUPPLEMENTARY TABLE S1. Climate types of sampled sites of NMNMSS in 30 PLADs and representative cities

No	PLADs	Climate types		Representative cities		
1	Anhui	C	Cfa	Hefei	Wuhu	Anqing
2	Anhui	C	Cwa	Huainan	Fuyang	Suzhou
3	Beijing	B, D	BSk, Dwa	Beijing		
4	Chongqing	C	Cfa, Cwa	Chongqing		
5	Fujian	C	Cfa	Fuzhou	Sanming	Zhangzhou
6	Gansu	B	BSk	Lanzhou	Pingliang	Qingyang
7	Gansu	B	BWk	Baiyin		
8	Gansu	D	Dwb	Pingliang		
9	Gansu	C	Cwa	Longnan		
10	Guangdong	C	Cfa	Shaoguan	Meizhou	Qingyuan
11	Guangdong	C	Cwa	Foshan	Maoming	Jieyang
12	Guangxi	C	Cwa	Nanning	Beihai	Fangchenggang
13	Guangxi	C	Cfa	Liuzhou	Guilin	Wuzhou
14	Guizhou	C	Cfa	Guiyang	Zunyi	Tongren
15	Guizhou	C	Cwa	Guiyang	Bijie	
16	Guizhou	C	Cwb	Liupanshui	Qianxinan	
17	Hainan	A	Aw	Haikou	Sanya	
18	Hainan	A	Am	Qionghai	Ding'an	
19	Hebei	B	BSk	Shijiazhuang	Xingtai	Baoding

Continued

No	PLADs	Climate types		Representative cities		
20	Hebei	D	Dwa	Tangshan	Qinhuangdao	Handan
21	Heilongjiang	D	Dwa	Harbin	Qiqihar	
22	Heilongjiang	D	Dwb	Jiamusi	Mudanjiang	Shuangyashan
23	Henan	C	Cwa	Zhengzhou	Kaifeng	Luoyang
24	Henan	D	Dwa	Anyang		
25	Henan	B	BSk	Jiyuan		
26	Hubei	C	Cfa	Wuhan	Xiangyang	Jingmen
27	Hubei	C	Cwa	Shiyan	Yichang	Enshi
28	Hunan	C	Cfa	Changsha	Zhuzhou	Xiangtan
29	Inner Mongolia	B	BSk	Huhhot	Ordos	Bayan Nur
30	Inner Mongolia	D	Dwa	Huhhot	Hinggan	
31	Inner Mongolia	D	Dwb	Hulun Buir		
32	Jiangsu	C	Cfa	Nanjing	Wuxi	Nantong
33	Jiangsu	C	Cwa	Xuzhou	Lianyungang	Yancheng
34	Jiangxi	C	Cfa	Nanchang	Jingdezhen	Pingxiang
35	Jilin	D	Dwa	Changchun	Jilin	Siping
36	Jilin	D	Dwb	Jilin	Baishan	Yanbian
37	Jilin	B	BSk	Baicheng		
38	Liaoning	D	Dwa	Shenyang	Dalian	Fushun
39	Liaoning	B	BSk	Chaoyang		
40	Ningxia	B	BWk	Yinchuan	Shizuishan	Wuzhong
41	Ningxia	B	BSk	Wuzhong	Guyuan	Zhongwei
42	Ningxia	D	Dwb	Guyuan		
43	Qinghai	B	BSk	Xining	Hainan	
44	Qinghai	D	Dwb	Haidong		
45	Shaanxi	C	Cwa	Xi'an	Baoji	Hanzhong
46	Shaanxi	B	BSk	Weinan	Yulin	
47	Shandong	D	Dwa	Jinan	Weifang	Weihai
48	Shandong	C	Cwa	Yantai	Rizhao	
49	Shanghai	C	Cfa	Shanghai		
50	Shanxi	B	BSk	Taiyuan	Jincheng	Shuozhou
51	Shanxi	D	Dwa	Yangquan	Changzhi	Yuncheng
52	Sichuan	C	Cwa	Chengdu	Zigong	Deyang
53	Sichuan	C	Cwb	Liangshan		
54	Tianjing	B, D	BSk, Dwa	Tianjing		
55	Xinjiang	D	Dfa	Urumqi	Lli	
56	Xinjiang	B	BSk	Urumqi	Changji	Lli
57	Xinjiang	B	BWk	Turpan	Bayingol	Kizilsu Krigiz
58	Yunnan	C	Cwb	Kunming	Qujing	
59	Yunnan	C	Cwa	Yuxi	Puer	Wenshan
60	Zhejiang	C	Cfa	Hangzhou	Ningbo	Wenzhou

Abbreviation: NMNMSS=National Maternal Near Miss Surveillance System；PLADs=provincial level administration divisions; A=Tropical; Am=Tropical-monsoon; Aw=Tropical-savannah; B=Arid; BSk=Arid-steppe-cold; BWk=Arid-desert-cold; C=Temperate; Cfa=Temperate-fully humid-hot summer; Cwa=Temperate-dry winter-hot summer; Cwb=Temperate-dry winter-warm summer; D=Cold; Dfa=Cold-fully humid-hot summer; Dwa=Cold-dry winter-hot summer; Dwb=Cold-dry winter-warm summer.

Methods and Applications

Nowcasting and Forecasting Seasonal Influenza Epidemics — China, 2022–2023

Zhanwei Du[1,2]; Zengyang Shao[2]; Xiao Zhang[2]; Ruohan Chen[2]; Tianmu Chen[3]; Yuan Bai[1,2]; Lin Wang[4]; Eric H. Y. Lau[5]; Benjamin J. Cowling[1,2,#]

ABSTRACT

Background: Seasonal influenza resurged in China in February 2023, causing a large number of hospitalizations. While influenza epidemics occurred across China during the coronavirus disease 2019 (COVID-19) pandemic, the relaxation of COVID-19 containment measures in December 2022 may have contributed to the spread of acute respiratory infections in winter 2022/2023.

Methods: Using a mathematical model incorporating influenza activity as measured by influenza-like illness (ILI) data for northern and southern regions of China, we reconstructed the seasonal influenza incidence from October 2015 to September 2019 before the COVID-19 pandemic. Using this trained model, we predicted influenza activities in northern and southern China from March to September 2023.

Results: We estimated the effective reproduction number R_e as 1.08 [95% confidence interval (*CI*): 0.51, 1.65] in northern China and 1.10 (95% *CI*: 0.55, 1.67) in southern China at the start of the 2022–2023 influenza season. We estimated the infection attack rate of this influenza wave as 18.51% (95% *CI*: 0.00%, 37.78%) in northern China and 28.30% (95% *CI*: 14.77%, 41.82%) in southern China.

Conclusions: The 2023 spring wave of seasonal influenza in China spread until July 2023 and infected a substantial number of people.

INTRODUCTION

In China, influenza virus exhibited apparent seasonality before the coronavirus disease 2019 (COVID-19) pandemic but was suppressed by multifaceted control strategies during the COVID-19 pandemic (*1*). However, due to the substantially reduced pathogenicity of the new COVID-19 variants,

officials decided to adjust the response strategies (e.g., restricting testing coverage, shortening quarantine periods for inbound travelers, and suspending secondary contact tracing) to better balance public health and economic factors starting on November 11, 2022 (*2*); then, on December 7, 2022, control measures (e.g., the prohibition of regional mass testing and the implementation of home isolation or quarantine) were further relaxed (*3*).

During the COVID-19 pandemic, nonpharmaceutical interventions (NPIs) such as social distancing, school closures, bans on large gatherings and nonessential activities, stay-at-home orders, travel restrictions, wearing face masks, extensive testing, contact tracing, and isolation programs have all been successful in slowing the spread of the virus that causes COVID-19, thereby minimizing outbreaks and saving lives (*4–7*). In early 2020, NPIs were estimated to have reduced influenza activity in southern and northern China by 79.2% and 79.4%, respectively, in contrast with normal seasonal influenza activity (*8*). This outcome was undoubtedly positive, especially in the short term, as it reduced the spread of the virus and thus the number of infections. However, the reduced circulation of influenza may have negative consequences in the long term; for example, when fewer people have developed immunity to influenza, a population can be rendered slightly more vulnerable to infection in the following season (*9–10*).

In China, the national influenza vaccination coverage rate per year was particularly lower than that in other countries, at approximately 2.2% in 2014 (*11*), in contrast with 6.9% at the global scale (*12*). The lack of immune stimulation due to reduced circulation of influenza could result in a more severe outbreak in the following season, potentially leading to more hospitalizations and deaths (*10*). It is thus unsurprising that there was a large resurgence of influenza B and influenza A activity in China in July 2021 and June 2022 in Shanghai, respectively (*1*).

The eventual cancellation of COVID-19-related

NPIs (e.g., the prohibition of regional mass testing and the implementation of home isolation or quarantine) in China on December 7, 2022 (*3*) led to an unprecedentedly large Omicron wave in December 2022 together with a sharp increase in influenza incidence in February 2023 (*13*). As of March 12, 2023, 807 outbreaks had been detected in China (*14*). For improving the surveillance and early warning systems for influenza epidemics, in this study, we projected the influenza incidence and quantified the influenza transmission dynamics (e.g., attack rate, peak timing, and peak value) in northern and southern China from October 2022 to September 2023 (epidemiological year 2022–2023) using a mathematical compartmental model informed by influenza data from 2015 to 2019.

METHODS

We collected weekly influenza surveillance data from the Chinese National Influenza Center for northern and southern China from 2015 to 2023 (*15*). To map the influenza-like illness positive (ILI+) to the weekly symptomatic incidence of the general population, we optimized the health care seeking rate μ with a value from 0 to 1 with steps of 0.1; the least mean square error (MSE) of ILI+ was between the observation and mean estimates of 100 simulations of the fitting and forecast results for 2015–2019 and 2022–2023. The influenza season was defined following reference (ref.) (*16*).

We characterized influenza transmission in the population using a susceptible-symptomatic-asymptomatic-recovered-hospitalized-dead (SYARHD) model and used this model to simulate influenza transmission dynamics per season. To forecast influenza activity, we used the ensemble adjustment Kalman filter (EAKF) to infer the varying transmission coefficients in the mathematical transmission model following the parameter setting in ref. (*17–19*). We replayed the historical infection pattern with the inferred transmission rates to validate the effectiveness of model calibration. When simulating influenza activity in the future season, we set the transmission rates at time t as the average of the transmission rates at time t in the previous four influenza seasons (2015–2016, 2016–2017, 2017–2018, and 2018–2019). By doing so, we could simulate the influenza infection pattern for different situations (i.e., various proportions of the susceptible population). By using the distribution of (β_t) inferred by EAKF, we derived the 95% confidence interval (*CI*) of the number of new infections each week. Then, we aggregated the new infections in the whole flu season and calculated the attack rate as the proportion of the population that was infected.

RESULTS

According to the influenza surveillance data from the Chinese National Influenza Center (*15*), influenza activity continued to increase in February 2023 after the sudden relaxation of COVID-19 control measures; consequently, among the eight study years, the highest influenza activity was observed in 2023, followed by 2020, and the lowest activity was observed in 2021, with no apparent seasonality. In contrast to that in northern China, the influenza activity in southern China was more serious in the summer of 2022. In this period, the ILI+ and influenza-like illness (ILI) in southern China were 23.90 per 1,000 and 75.41 per 1,000 persons, respectively, which were higher than those in northern regions (4.44 per 1,000 and 27.77 per 1,000 persons, respectively). The ILI had a rebound increase in December 2022 and peaked at 130.96 per 1,000 and 86.25 per 1,000 persons in the southern and northern regions, respectively, during the Omicron variant outbreak in China, and resulted in notably increasing ILI cases compared with any other period. In February 2023, ILI+ had the highest values of 54.39 per 1,000 and 51.41 per 1,000 persons in the northern and southern regions, respectively.

To validate the epidemic models used in this study, we performed model calibration for influenza outbreaks in North and South China over five influenza seasons (2015–2016, 2016–2017, 2017–2018, 2018–2019, and 2022–2023). Informed by ILI+ (Figure 1), we used the EAKF algorithm (Methods) to infer the transmission rates in previous influenza seasons and replayed the historical infection pattern in the northern and southern regions of China (Figures 2–3).

We projected the influenza activity between October 9, 2022, and October 1, 2023 (Figure 4), with the transmission rate as the fitted value in the 2015–2019 seasons (Figure 3). During the study period, we estimated that the attack rates were 18.51% (95% *CI*: 0.00%, 37.78%) and 28.30% (95% *CI*: 14.77%, 41.82%) in northern and southern China, respectively. The influenza incidence was estimated to peak on March 12, 2023, and March 19, 2023, in northern and southern China, with ILI+ values of 61.28 (95%
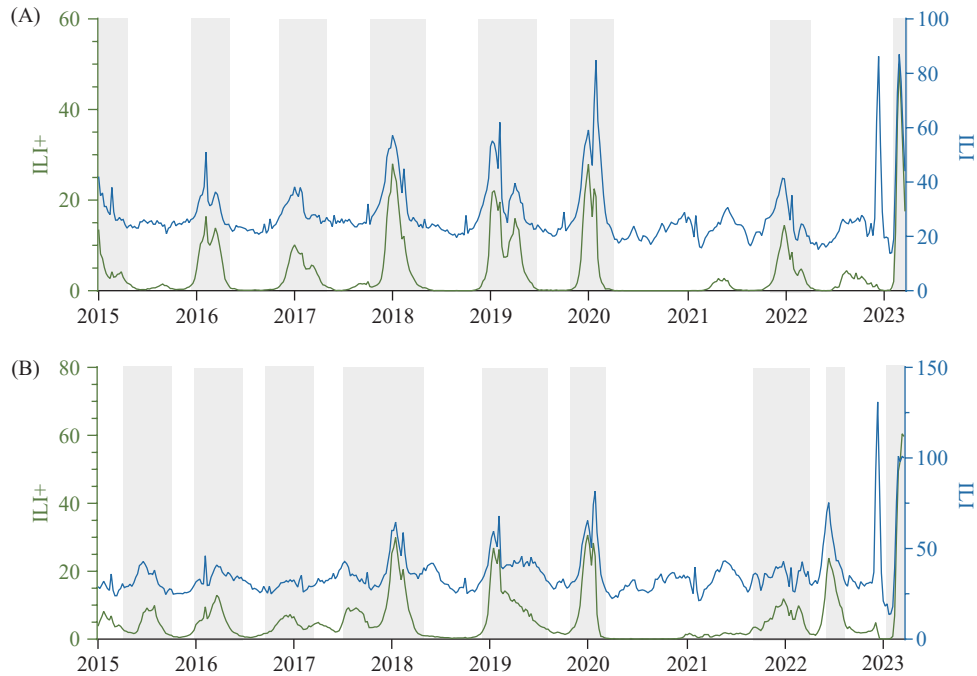
FIGURE 1. ILI and ILI+ in (A) northern China and (B) southern China.
Note: We estimated seasonal ILI+ (*20*) in northern and southern regions by multiplying the activities of ILI by public health laboratory estimates of percent positive influenza tests from the China CDC surveillance system for the 2015–2022 seasons. Gray shading represents the influenza seasons (*16*).
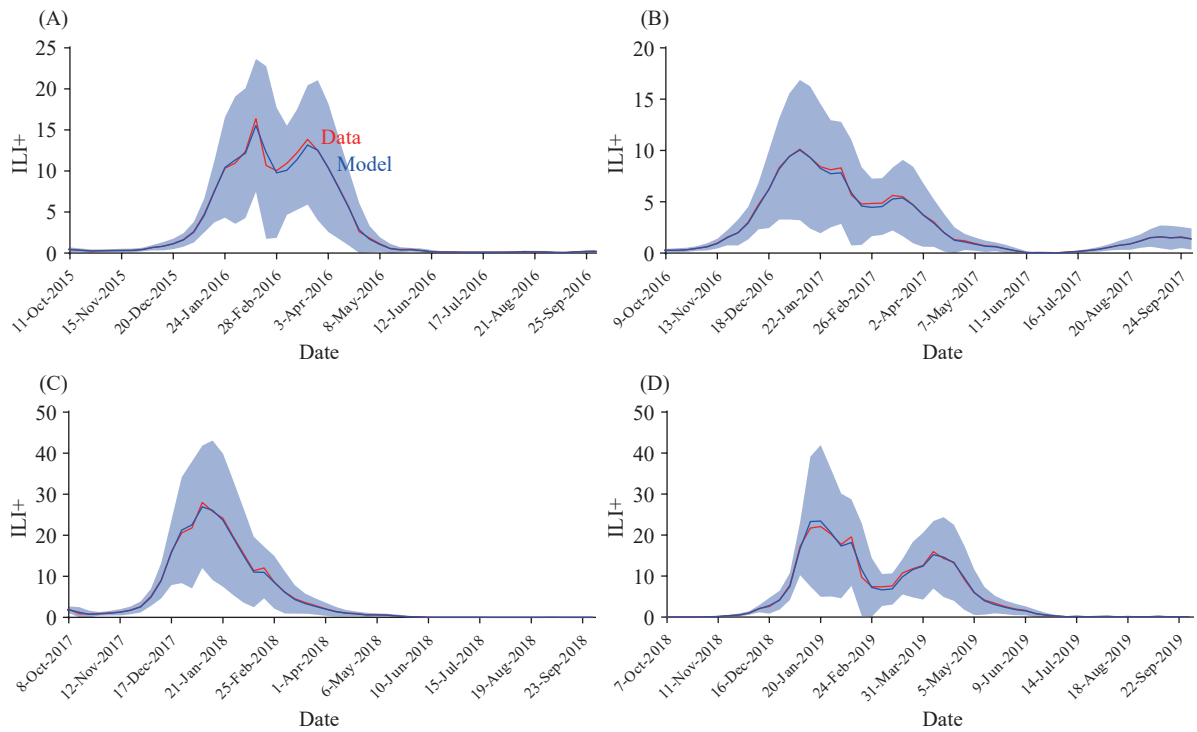Abbreviation: ILI+=Influenza-like illness positive; ILI=Influenza-like illness.

FIGURE 2. Reconstruction fit of ILI+ between 2015 and 2019 in northern regions. (A) 2015–2016; (B) 2016–2017; (C) 2017–2018; (D) 2018–2019.
Note: Blue lines and shaded areas indicate the mean and 95% *CI* of the estimation. The red line indicates the data.
Abbreviation: ILI+=Influenza-like illness positive; ILI=Influenza-like illness; *CI*=confidence interval.
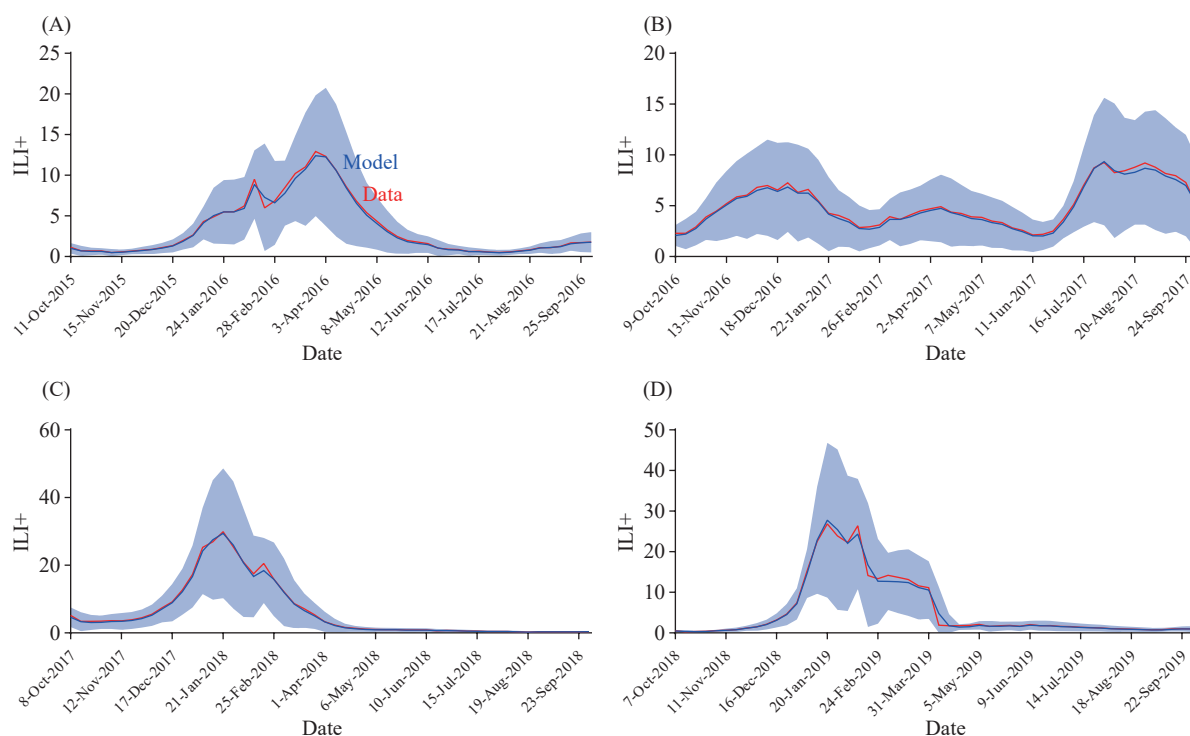
FIGURE 3. Reconstruction of ILI+ between 2015 and 2019 in southern regions. (A) 2015–2016; (B) 2016–2017; (C) 2017–2018; (D) 2018–2019.

Note: Blue lines and shaded areas indicate the mean and 95% *CI* of the estimation. The red line indicates the data.

Abbreviation: ILI+=Influenza-like illness positive; ILI=Influenza-like illness; *CI*=confidence interval.

CI: 0, 160.87) and 66.04 (95% *CI*: 0, 161.09), respectively, and the outbreaks were predicted to end on June 18 and July 23, 2023, in northern and southern China, respectively. For the influenza season of 2022–2023, the attack rate was estimated to exceed 5% in northern and southern China for 72% and 83% of the epidemics, respectively.

The effective reproduction number R_e between October 9, 2022, and October 1, 2023, started at 1.08 (95% *CI*: 0.51, 1.65) and 1.10 (95% *CI*: 0.55, 1.67) and reached as high as 2.13 (95% *CI*: 1.56, 2.70) on February 26, 2023, and 2.44 (95% *CI*: 1.86, 3.01) on February 26, 2023, while the mean estimates were 0.93 (95% *CI*: 0.35, 1.51) and 0.96 (95% *CI*: 0.44, 1.49), respectively, in northern and southern China. In contrast, the mean estimate was 0.97 (95% *CI*: 0.96, 0.98) and 0.99 (95% *CI*: 0.98, 1.00), with peak values of 1.60 (95% *CI*: 1.56, 1.65) and 1.42 (95% *CI*: 1.41, 1.43), for the period from October 2015 to September 2019 in northern and southern China, respectively.

The estimated proportions of the initially susceptible population (S_0) on October 9, 2022, were 0.73 and 0.76 in northern and southern China, respectively. Following the same R_e, a higher S_0 would cause both a higher ILI+ and attack rate. We further investigated the impact of susceptibility on the attack rate by varying S_0 from 50% to 80% across the transmission scenarios (Supplementary Figures S1–S2, available in https://weekly.chinacdc.cn/). In southern China, we estimated that the attack rates were 0.11% (95% *CI*: 0.04%, 0.19%), 0.45% (95% *CI*: 0%, 1.12%), 14.00% (95% *CI*: 3.37%, 24.62%), and 35.72% (95% *CI*: 18.21%, 53.24%) for S_0= 0.5, 0.6, 0.7, and 0.8, respectively. In northern China, we estimated that the attack rates were 0.18% (95% *CI*: 0.05%, 0.32%), 0.61% (95% *CI*: 0.00%, 1.26%), 10.27% (95% *CI*: 0.00%, 24.55%), and 42.54% (95% *CI*: 18.79%, 66.28%) for S_0= 0.5, 0.6, 0.7, and 0.8, respectively.

DISCUSSION

Infection with respiratory viruses, including influenza viruses and respiratory syncytial virus (RSV), typically occurs in seasonal patterns in China, with increased incidence during the cooler months of the year and around summer in southern China. However, due to the strict public health measures implemented during the COVID-19 pandemic, such as social distancing and wearing masks, the circulation of influenza was significantly reduced in 2020 and 2021.
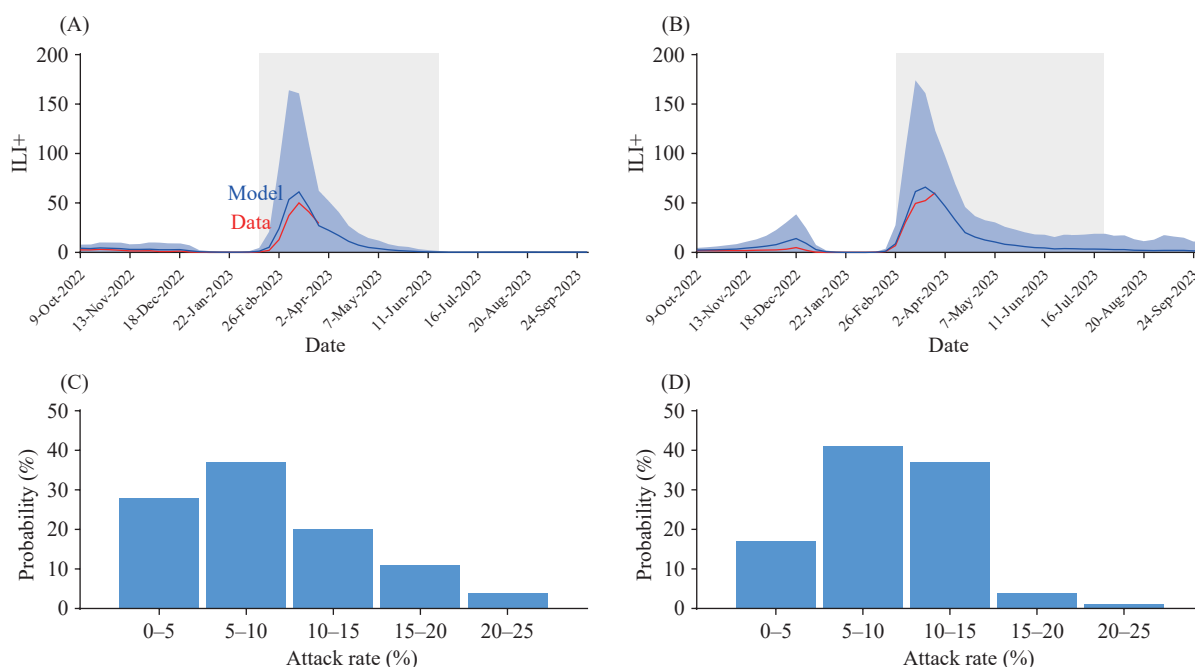
FIGURE 4. Projected ILI+ between October 9, 2022, and September 30, 2023. (A) The transmission rate in the 2022–2023 season in northern China, (B) the transmission rate in the 2022–2023 season in southern China; (C) probability distribution of the attack rate in northern China; (D) probability distribution of the attack rate in southern China.
Note: ILI+ is fitted before March 26, 2023, and projected after March 26 until September 30, 2023. We used the mean estimates of the four fitted transmission rates per week for the 2015–2016, 2016–2017, 2017–2018, and 2018–2019 seasons as the transmission rate for the same week in the 2022–2023 season. We ran 100 stochastic simulations and estimated the weekly incidence. Blue lines and shaded areas indicate the mean and 95% CI of the model, whereas the red line denotes the observations. Gray shading represents the influenza season (16). We estimated the attack rate for the influenza season for each of the 100 stochastic simulations and estimated the probability distribution.
Abbreviation: ILI+=Influenza-like illness positive; ILI=Influenza-like illness; CI=confidence interval.

With the gradual relaxation of COVID-19 NPIs in late 2020 and further relaxation after the COVID-19 Omicron wave in late 2022, influenza started to spread in the community. It is important to remain vigilant and track influenza development when it circulates, especially among vulnerable populations such as older adults and those with underlying health conditions. Although considerable uncertainty exists regarding cocirculating influenza variants, vaccines, and NPIs, we projected that influenza activities peaked in March 2023 in northern and southern China.

Influenza epidemiology is characterized by seasonality, which is influenced by population contact patterns, viral survival, and host immunity (21). In temperate climate zones, influenza seasons are generally synchronized and occur during winter (22). However, pandemics can occur when a new influenza virus emerges and spreads globally, causing severe illness, death, and significant social and economic disruption. Some influenza pandemics have had unusual patterns of illness, with out-of-season waves reported. For example, during the 1918 pandemic, there were three

waves of illness, with the first wave occurring in the spring of 1918, followed by a second, more severe wave in the fall of that year and a third wave in the winter and spring of 1919. The 2009 H1N1 pandemic also had an unusual pattern of illness, with a first wave occurring in the spring of 2009, followed by a larger second wave in the fall and winter of that year. These perturbations are typically limited to the first year of circulation of a pandemic virus (22).

Compared to previous influenza pandemics, recent influenza activity has been substantially disrupted by the COVID-19 pandemic. This pandemic has caused changes in contact patterns and mobility, which have affected the seasonal cycles of many infectious diseases globally, including influenza. When COVID-19 first emerged in 2020, there was little to no influenza activity in either hemisphere due to the reduction in human mobility and contact in response to COVID-19. However, influenza started to resurge in late 2021, with out-of-season activity in the Southern Hemisphere. A peak in weekly influenza cases was reported in Australia in June 2022, earlier than typical

and far exceeding the 5-year average (*23*). According to the March 20, 2023, World Health Organization update, influenza activity continued to decrease following the peak in late 2022 (*24*). In North America, most indicators of influenza activity were at end-of-season levels, while in Europe, overall influenza diagnoses decreased slightly, and influenza positivity rates decreased according to data from sentinel sites, although these values remained above the epidemic threshold at the regional level. In East Asia, the activity of influenza A (H1N1) pdm09, which was the predominant strain, steeply increased in China but decreased in the other reporting countries.

The rise in the prevalence of respiratory viruses may not solely be attributed to the relaxation of strict NPIs used during the pandemic and population behavioral changes in response to perceived levels of risk. Importantly, while COVID-19 has created many challenges, it has also highlighted the significance of maintaining good health and hygiene practices.

The influenza A (H1N1), A (H3N2) and B strains can cocirculate in an influenza season. According to the isolation and identification results for the influenza virus from the China CDC (*14*), nearly half of samples from infected individuals harbored B viruses between 2015 and 2019. However, more than 99% of virus-positive samples contained A viruses in 2023. Compared to influenza B, influenza A tends to be more transmissible (*25*) and more likely to cause a pandemic (*26*), which may have resulted in the higher peak in 2023 than before. In the summer of 2022, an H3N2 influenza outbreak occurred in southern regions and peaked on June 20, 2022, with an ILI+ of 23.9, while the maximum ILI+ in northern regions was only 4.44 for the same period. Although natural infection provides long-lived immunity (*27*) in southern regions, the estimated attack rate and S_0 in southern regions in 2022–2023 seasons are higher than that in northern regions.

For years, a global control strategy for influenza has been implemented based on regular vaccine strain updates, which are centered on the synchronicity of influenza circulation at the hemispheric level (*28*). The findings of this study have important practical implications for public health authorities. The return of influenza activity in 2021–2022 highlights the need for improved influenza vaccines and increased vaccination coverage. Public health authorities should prioritize the development and distribution of improved influenza vaccines and ensure that vaccination campaigns are widely promoted and accessible to all populations, particularly vulnerable groups such as older adults and those with underlying health conditions. Resource allocation should be carefully considered in the context of cocirculating influenza variants and the potential for pandemics. Public health authorities should prioritize the allocation of resources toward surveillance and early warning systems for influenza epidemics as well as the development and distribution of antiviral medications in addition to vaccine development and distribution. Given the limitations of this study, public health authorities should continue to monitor the situation closely and adjust their strategies accordingly. These strategies include ongoing surveillance of influenza activity, vaccine coverage and efficacy tracking, and evaluation of the impact of NPIs, such as social distancing and wearing masks, on influenza transmission.

The limitations of this study should be noted. Our model does not explicitly include contact patterns, mobility, vaccination or NPIs but captures these factors through our estimates of transmissibility. Second, we use weekly ILI+ and scaling factors to map ILI+ to the weekly symptomatic incidence of the general population from municipal-scale estimates to denote the transmission rate, which may bias the attack rate given the potential uncertainty in spatial heterogeneity.

CONCLUSION

Understanding influenza seasonality is important for predicting and preparing for future outbreaks. After the cancellation of COVID-19-related measures in China in December 2022, we expected that a significant increase in influenza activity would last for 4 months in northern and southern China starting from mid-February to mid-June 2023. Although pandemic influenza seasons can disrupt regular seasonal cycles, further research is needed to improve our understanding of influenza seasonality and the emergence of new viruses. This is a crucial time to initiate well-designed studies that can help us understand how seasonal factors, immunity, contact patterns, and infections interact.

Conflicts of interest: BJC has consulted for AstraZeneca, Fosun Pharma, GSK, Haleon, Moderna, Roche, and Sanofi Pasteur. The authors report no conflicts of interest.

Technology Commission of the Government of the Hong Kong Special Administrative Region and the Theme-based Research Scheme (T11-712/19-N) of the Research Grants Council of the Hong Kong SAR Government.

Corresponding author: Benjamin J. Cowling, bcowling@hku.hk.

---

¹ WHO Collaborating Center for Infectious Disease Epidemiology and Control, School of Public Health, LKS Faculty of Medicine, The University of Hong Kong, Hong Kong Special Administrative Region, China; ² Laboratory of Data Discovery for Health Limited, Hong Kong Science and Technology Park, Hong Kong Special Administrative Region, China; ³ State Key Laboratory of Molecular Vaccinology and Molecular Diagnostics, School of Public Health, Xiamen University, Xiamen City, Fujian Province, China; ⁴ Department of Genetics, University of Cambridge, Cambridge, UK; ⁵ Institute for Health Transformation & School of Health & Social Development, Deakin University, Melbourne, Australia.

REFERENCES

1. Liu PC, Xu J. Resurgence of influenza virus activity during COVID-19 pandemic in Shanghai, China. J Infect 2023;86(1):66 – 117. http://dx.doi.org/10.1016/j.jinf.2022.09.025.
2. Huaxia. China Focus: China releases measures to optimize COVID-19 response. 2022. https://english.news.cn/20221111/d4399114a082438eaac32d08a02bf58d/c.html. [2023-2-4].
3. Huaxia. China Focus: COVID-19 response further optimized with 10 new measures. 2022. https://english.news.cn/20221207/ca014c043bf24728b8dcbc0198565fdf/c.html. [2023-2-4].
4. Lai SJ, Ruktanonchai NW, Zhou LC, Prosper O, Luo W, Floyd JR, et al. Effect of non-pharmaceutical interventions to contain COVID-19 in China. Nature 2020;585(7825):410 – 3. http://dx.doi.org/10.1038/s41586-020-2293-x.
5. University of Oxford. Coronavirus government response tracker. 2020. https://www.bsg.ox.ac.uk/research/research-projects/coronavirus-government-response-tracker. [2020-7-17].
6. Wang XT, Pasco RF, Du ZW, Petty M, Fox SJ, Galvani AP, et al. Impact of social distancing measures on coronavirus disease healthcare demand, Central Texas, USA. Emerg Infect Dis 2020;26(10):2361 – 9. http://dx.doi.org/10.3201/eid2610.201702.
7. Du ZW, Xu XK, Wang L, Fox SJ, Cowling BJ, Galvani AP, et al. Effects of proactive social distancing on COVID-19 outbreaks in 58 cities, China. Emerg Infect Dis 2020;26(9):2267 – 9. http://dx.doi.org/10.3201/eid2609.201932.
8. Feng LZ, Zhang T, Wang Q, Xie YR, Peng ZB, Zheng JD, et al. Impact of COVID-19 outbreaks and interventions on influenza in China and the United States. Nat Commun 2021;12(1):3249. http://dx.doi.org/10.1038/s41467-021-23440-1.
9. Cohen R, Ashman M, Taha MK, Varon E, Angoulvant F, Levy C, et al. Pediatric Infectious Disease Group (GPIP) position paper on the immune debt of the COVID-19 pandemic in childhood, how can we fill the immunity gap? Infect Dis Now 2021;51(5):418-23. http://dx.doi.org/10.1016/j.idnow.2021.05.004.
10. Ali ST, Lau YC, Shan SW, Ryu S, Du ZW, Wang L, et al. Prediction of upcoming global infection burden of influenza seasons after relaxation of public health and social measures during the COVID-19 pandemic: a modelling study. Lancet Glob Health 2022;10(11):e1612 – 22. http://dx.doi.org/10.1016/S2214-109X(22)00358-8.
11. Yang J, Atkins KE, Feng LZ, Pang MF, Zheng YM, Liu XX, et al. Seasonal influenza vaccination in China: landscape of diverse regional reimbursement policy, and budget impact analysis. Vaccine 2016;34(47):5724 – 35. http://dx.doi.org/10.1016/j.vaccine.2016.10.013.
12. Palache A, Rockman S, Taylor B, Akcay M, Billington JK, Barbosa P, et al. Vaccine complacency and dose distribution inequities limit the benefits of seasonal influenza vaccination, despite a positive trend in use. Vaccine 2021;39(41):6081 – 7. http://dx.doi.org/10.1016/j.vaccine.2021.08.097.
13. Zeng XX, Xie YR, Yang XK, Peng ZB, Tang J, Yang L, et al. SARS-CoV-2 surveillance through China influenza surveillance information system — China, December 1, 2022 to February 12, 2023. China CDC Wkly 2023;5(7):152 – 8. http://dx.doi.org/10.46234/ccdcw2023.027.
14. Chinese National Influenza Center. China influenza weekly report as of March 2023. https://ivdc.chinacdc.cn/cnic/zyzx/lgzb/202303/t20230316_264314.htm. [2023-3-16]. (In Chinese).
15. Chinese National Influenza Center. Chinese national influenza center. https://ivdc.chinacdc.cn/cnic/en/Surveillance/. [2023-3-24].
16. Yang W, Cowling BJ, Lau EHY, Shaman J. Forecasting influenza epidemics in Hong Kong. PLoS Comput Biol 2015;11(7):e1004383. http://dx.doi.org/10.1371/journal.pcbi.1004383.
17. Pei S, Teng X, Lewis P, Shaman J. Optimizing respiratory virus surveillance networks using uncertainty propagation. Nat Commun 2021;12(1):222. http://dx.doi.org/10.1038/s41467-020-20399-3.
18. Du ZW, Fox SJ, Ingle T, Pignone MP, Meyers LA. Projecting the combined health care burden of seasonal influenza and COVID-19 in the 2020–2021 season. MDM Policy Pract 2022;7(1):23814683221084631. http://dx.doi.org/10.1177/23814683221084631.
19. Borchering RK, Gunning CE, Gokhale DV, Weedop KB, Saeidpour A, Brett TS, et al. Anomalous influenza seasonality in the United States and the emergence of novel influenza B viruses. Proc Natl Acad Sci USA 2021;118(5):e2012327118. http://dx.doi.org/10.1073/pnas.2012327118.
20. Wu P, Presanis AM, Bond HS, Lau EHY, Fang VJ, Cowling BJ. A joint analysis of influenza-associated hospitalizations and mortality in Hong Kong, 1998-2013. Sci Rep 2017;7(1):929. http://dx.doi.org/10.1038/s41598-017-01021-x.
21. Tamerius J, Nelson MI, Zhou SZ, Viboud C, Miller MA, Alonso WJ. Global influenza seasonality: reconciling patterns across temperate and tropical regions. Environ Health Perspect 2011;119(4):439 – 45. http://dx.doi.org/10.1289/ehp.1002383.
22. Lee SS, Viboud C, Petersen E. Understanding the rebound of influenza in the post COVID-19 pandemic period holds important clues for epidemiology and control. Int J Infect Dis 2022;122:1002 – 4. http://dx.doi.org/10.1016/j.ijid.2022.08.002.
23. Australian Government Department of Health and Aged Care. Influenza surveillance program. 2023. https://www.health.gov.au/our-work/influenza-surveillance-program?utm_source=health.gov.au&utm_medium=callout-auto-custom&utm_campaign=digital_transformation. [2023-3-22].
24. WHO. Global influenza programme. 2023. https://www.who.int/teams/global-influenza-programme/surveillance-and-monitoring/influenza-updates/current-influenza-update. [2023-3-22].
25. Dai HY, Zhou N, Chen MX, Li GQ, Yu X, Su Y, et al. Assess transmissibility of different influenza subtypes: based on a SEIABR model. Infect Genet Evol 2022;103:105319. http://dx.doi.org/10.1016/j.meegid.2022.105319.
26. CDC. Pandemic influenza. 2020. https://www.cdc.gov/flu/pandemic-resources/index.htm. [2023-3-23].
27. Krammer F. The human antibody response to influenza A virus infection and vaccination. Nat Rev Immunol 2019;19(6):383 – 97. http://dx.doi.org/10.1038/s41577-019-0143-6.
28. Saha S, Chadha M, Al Mamun A, Rahman M, Sturm-Ramirez K, Chittaganpitch M, et al. Influenza seasonality and vaccination timing in tropical and subtropical areas of southern and south-eastern Asia. Bull World Health Organ 2014;92(5):318 – 30. http://dx.doi.org/10.2471/BLT.13.124412.

SUPPLEMENTARY MATERIAL

Data

Weekly influenza surveillance data were obtained from the Chinese National Influenza Center (*1*) for northern and southern China from 2015 to 2023. The data reported each week included the number of influenza-like illness (ILI) cases at the sentinel hospitals and the number of positive cases of influenza A (H1N1, H3N2, and pdmH1) and influenza B (Yamagata and Victoria) that were examined in a laboratory. We calculated the weekly incidence rate of influenza by multiplying the ILI rate by the positive rate of viral detection.

The influenza season was defined in the following refference (*2*). The onset of influenza seasons refers to the first of three consecutive weeks when influenza-like illness positive (ILI+) records exceeded a prescribed baseline (40% quantile of the nonzero ILI+ records). The end of the season refers to the first of two consecutive weeks with ILI+ below the baseline following the onset of the season.

Since ILI+ was calculated according to the ILI and laboratory-positive rate, it only represents the influenza-positive proportion of the health care-seeking population. Therefore, in our study, we assumed a health care seeking rate μ to map ILI+ to the weekly symptomatic incidence of the general population and then to obtain the weekly incidence of the general population based on the weekly symptomatic incidence and the symptomatic proportion. For the optimal value of μ, we chose a value from 0 to 1 with steps of 0.1; the least mean square error (MSE) of ILI+ was between the observation and mean estimates of 100 simulations of the fitting and forecast results for 2015–2019 and 2022–2023.

Transmission Model

We characterized influenza transmission in the population using a susceptible-symptomatic-asymptomatic-recovered-hospitalized-dead (SYARHD) model and used this model to simulate influenza transmission dynamics per season. The model equations were as follows:

$$S_{t+1} = S_t - \beta_t \times S_t \times (Y_t + \omega \times A_t) + \gamma \times R_t \tag{1}$$

$$Y_{t+1} = Y_t + \sigma \times \beta_t \times S_t \times (Y_t + \omega \times A_t) - \alpha \times Y_t - \delta_2 \times Y_t \tag{2}$$

$$A_{t+1} = A_t + (1 - \sigma) \times \beta_t \times S_t \times (Y_t + \omega \times A_t) - \delta_1 \times A_t \tag{3}$$

$$R_{t+1} = R_4 + \delta_1 \times A_t + \delta_2 \times Y_t + \delta_3 \times H_t - \gamma \times R_t \tag{4}$$
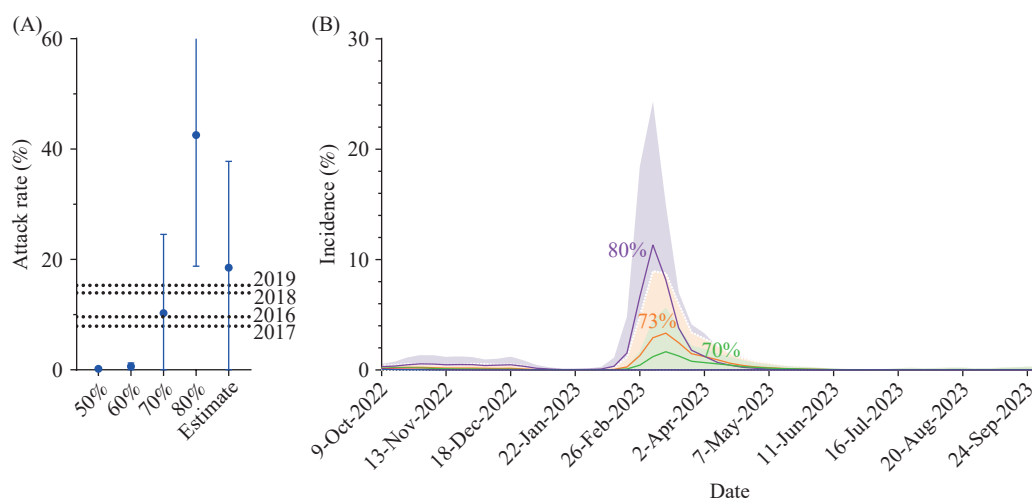
SUPPLEMENTARY FIGURE S1. Projected attack rates for the influenza outbreak in northern regions.
Note: Panel (A) is the estimated attack rates with the mean and 95% confidence interval (*CI*) between October 9, 2022, and September 30, 2023 across five transmission scenarios: 50%, 60%, 70%, 80% and our best estimate (73%) of the population initially susceptible on October 9, 2022. Panel (B) is the estimated incidence (%) of influenza infections across four scenarios. Black dotted horizontal lines correspond to attack rates for the same period during the 2015–2019 influenza seasons. We ran 100 stochastic simulations. Lines and shaded areas indicate the mean and 95% *CI* of the model.
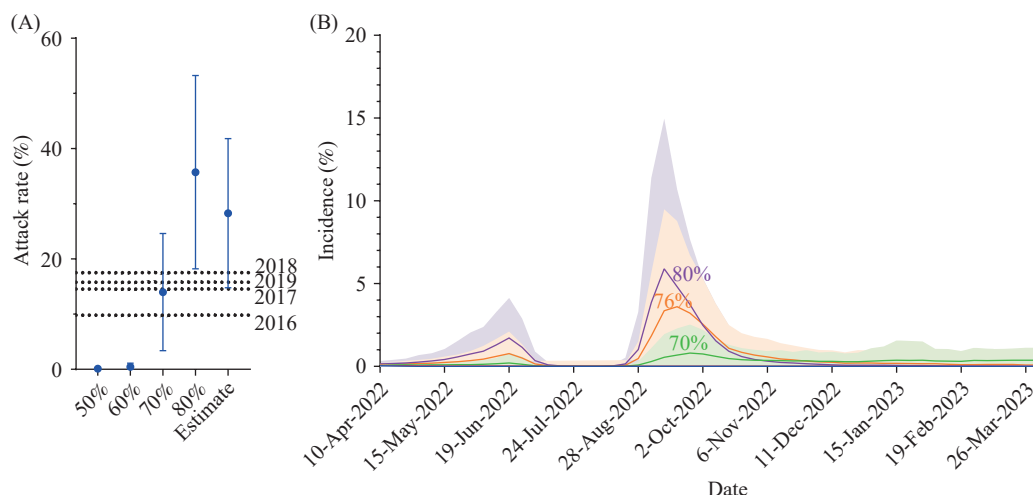
SUPPLEMENTARY FIGURE S2. Projected attack rates for the influenza outbreak in southern regions.

Note: Panel (A) estimated attack rates with the mean and 95% confidence interval (*CI*) between October 9, 2022, and September 30, 2023, across five transmission scenarios: 50%, 60%, 70%, 80% and our best estimate (78%) of the population initially susceptible on October 9, 2022. Panel (B) estimated incidence (%) of influenza infections across four scenarios. Black dotted horizontal lines correspond to attack rates for the same period during the 2015–2019 influenza seasons. We ran 100 stochastic simulations. Lines and shaded areas indicate the mean and 95% *CI* of the model.

$$H_{t+1} = H_t + \alpha \times Y_t - \delta_y \times H_t - \epsilon \times H_t \tag{5}$$

$$D_{t+1} = D_t + \epsilon \times H_t \tag{6}$$

Following infection at time t, susceptible individuals (S_t) enter an infectious state (symptomatic Y_t and asymptomatic A_t), in which a fraction of infected patients recover (R_t) at rate δ. Those recovered patients remain protected from future infection for the duration of $1/\gamma$ on average.

To forecast influenza activity, we used the ensemble adjustment Kalman filter (EAKF) to infer the varying transmission coefficient β_t at time t in the mathematical transmission model as well as the proportion of daily susceptible population S_t and infected population I_t and A_t. We set $\sigma = 0.55$, $\delta_1 = 1/3$, $\delta_2 = 1/5$, $\delta_3 = 0.9981$, $\alpha = 0.0146$, $\gamma = 1/(4 \times 365)$, $\omega = 0.36$, and $\varepsilon = 0.0019$ following refs. (3–5). The effective reproduction number (R_e) at time t was calculated as follows:

$$R_t(t) = S_t \times \beta_t \times \left(\frac{\sigma}{\delta_2 + \alpha} + \omega \times \frac{1 - \sigma}{\delta_1} \right) \tag{7}$$

In each influenza season, we hierarchically inferred S_0 and β_t. For a given S_0, β_t was calibrated over time using EAKF. During the fitting period between 2015 and 2019, the initial S_0 values were drawn using latin hypercube sampling (LHS) from the range [0.65, 0.75] with 100 stochastic simulations (3). To forecast the influenza activity between October 9, 2022, and September 30, 2023, we chose a value from 0.65 to 1 with steps of 0.01; the least mean square error (MSE) of ILI+ was between the observation and mean estimates of 100 stochastic simulations.

In the parameter calibration of β_t, EAKF uses a group of particles (with population size N^p) to approximate the distribution of β_t. Specifically, one particle contains a specific combinatorial value of the hidden variables, for instance (β^i_t), and a group of particles are regarded as N^p random samples from the underlying distribution of these hidden variables (β_t). We set the number of particles N^p to 10,000.

To infer the hidden variables, EAKF assigns a weighting w_t to each particle according to its likelihood of generating the observed incidence. We model the influenza activity using the SIRS model on a daily basis, while the influenza incidence data are reported weekly. To align our model output with the reported data, we aggregate the daily new infection simulated by the SIRS model to weekly incidence, $dI_w = \sum_{t=d}^{d+6} \beta_t \times S_t \times (I_t + A_t)$, where d is the first day of week w. That is, we only calculate weightings for the end day of each week. The assigned weighting w_t is negatively proportional to the distance between the modeled weekly incidence and the observed ILI+ weekly incidence O_w, which we model using the Gaussian likelihood function: $w^i_t \propto \mathbb{N}\left(dI^i_w \middle| O_w, \Omega\right)$, where $\Omega = 0.25 \times O_w$. In the simulation of influenza activity at the next time step $t + 1$, EAFK draws one particle from the particle group at

time step $t+1$ with probability $w^j{}_t, j \in [1, N^p]$ and propagates to the next time step $t+1$ with the SIRS transmission model using the value of the drawn particle ($\beta^j{}_t$).

We replayed the historical infection pattern with the inferred transmission rates to validate the effectiveness of model calibration. When simulating the influenza activity in the future season, we set the transmission rates at time t as the average of the transmission rates at time t in the previous four influenza seasons (2015–2016, 2016–2017, 2017–2018, and 2018–2019). By doing so, we simulated the influenza infection pattern for different situations (i.e., various proportions of a susceptible population). By using the distribution of (β_t) inferred by EAKF, we derived the 95% confidence interval of the number of new infections each week. Then, we aggregated the new infections for the whole flu season and calculated the attack rate as the proportion of the population that was infected.

REFERENCES

1. Chinese National Influenza Center. Chinese national influenza center. https://ivdc.chinacdc.cn/cnic/en/Surveillance/. [2023-3-24].
2. Yang W, Cowling BJ, Lau EHY, Shaman J. Forecasting influenza epidemics in Hong Kong. PLoS Comput Biol 2015;11(7):e1004383. http://dx.doi.org/10.1371/journal.pcbi.1004383.
3. Pei S, Teng X, Lewis P, Shaman J. Optimizing respiratory virus surveillance networks using uncertainty propagation. Nat Commun 2021;12(1):222. http://dx.doi.org/10.1038/s41467-020-20399-3.
4. Du ZW, Fox SJ, Ingle T, Pignone MP, Meyers LA. Projecting the combined health care burden of seasonal influenza and COVID-19 in the 2020-2021 season. MDM Policy Pract 2022;7(1):23814683221084631. http://dx.doi.org/10.1177/23814683221084631.
5. Borchering RK, Gunning CE, Gokhale DV, Weedop KB, Saeidpour A, Brett TS, et al. Anomalous influenza seasonality in the United States and the emergence of novel influenza B viruses. Proc Natl Acad Sci USA 2021;118(5):e2012327118. http://dx.doi.org/10.1073/pnas.2012327118.

Vital Surveillances

eALT-F: A New Non-Invasive Staging Method to Identify Medium to High-Risk Patients with HCC from Ultra-High HBV Viral Load Population — China, 2010–2023

Jiarui Zheng[1,&]; Xiaoxiao Wang[2,&,#]; Zilong Wang[2]; Linxiang Huang[1]; Yandi Xie[1]; Suzhen Jiang[1]; Bo Feng[1,#]

ABSTRACT

Background: The objective of this study was to examine the clinical characteristics of individuals with ultra-high hepatitis B virus (HBV) viral load and develop a novel staging method for chronic hepatitis B (CHB) that can more effectively identify patients with medium to high hepatocellular carcinoma (HCC) risk.

Methods: A total of 2,118 patients with HBV DNA >1×10^7 IU/mL who visited Peking University People's Hospital between January 2010 and March 2023 were enrolled retrospectively. Clinical data from the first visit were obtained and analyzed. The traditional phases and new 'eALT-F' stages were compared to evaluate the risk of HCC.

Results: In the overall patients, more than one-third of the patients were under 30 years old. Additionally, a small proportion of older people (>60 years) also had ultra-high HBV viral load (4.3%). 9.1% and 6.7% of individuals with ultra-high HBV viral load showed FIB-4>3.25 and aMAP≥50, respectively. In the traditional stages of CHB, which are based on HBeAg and alanine aminotransferase (ALT) [the upper limit of normal (ULN) ALT level at 40 IU/L for both men and women], regardless of phase, a certain proportion of patients were at risk of developing HCC (4.1%, 6.4%, 25.0%, and 20.3%). However, in the new 'eALT-F' stages, which are based on HBeAg, ALT (the ULN of ALT level at 30 IU/L for men and 19 IU/L for women), and/or FIB-4 levels (>1.45), aMAP≥ 50 was only observed in chronic hepatitis patients with positive or negative HBeAg (6.4% and 22.1%, respectively).

Conclusions: The 'eALT-F' staging method, based on HBeAg, ALT (males: the ULN of ALT was 30 IU/L, females: 19 IU/L) and/or FIB-4 levels, was more effective in identifying medium to high-risk patients with HCC from patients with ultra-high HBV viral load than the traditional staging methods.

INTRODUCTION

Chronic hepatitis B virus (HBV) infection remains a major public health concern worldwide. According to the World Health Organization (WHO), there are approximately 296 million individuals with chronic HBV infection globally, resulting in liver-related diseases such as cirrhosis, hepatocellular carcinoma (HCC), and liver failure, which lead to the deaths of an estimated 820,000 patients annually (*1*). Despite the successful popularization of the hepatitis B vaccine, there is still a prevalence of 5%–6% of individuals with positive HBsAg in the general population in China (*1*). Therefore, chronic HBV infection poses a serious socio-economic burden. Achieving the WHO's objective of eliminating viral hepatitis by 2030 remains a challenging responsibility, involving inhibiting HBV transmission and treating or even curing individuals with chronic HBV infection.

Based on markers of HBV infection, such as HBsAg, HBeAg, HBV DNA level, alanine aminotransferase (ALT) level, and liver pathological features, the natural history of chronic HBV infection can be categorized into four classical phases, including HBeAg-positive chronic HBV infection (immune-tolerant phase, IT phase), HBeAg-positive chronic hepatitis B (immune activation phase), HBeAg-negative chronic HBV infection (low replication phase), and HBeAg-negative chronic hepatitis B (reactivation phase) (*2*). Individuals in the HBeAg-positive chronic HBV infection phase are often accompanied by higher levels of HBV DNA. Previous studies demonstrated that an elevated HBV viral load was associated with an increased risk of HCC occurrence (*3–4*). Additionally, a higher HBV viral load has been identified as an independent risk factor for HCC recurrence, specifically after liver resection, transplantation, or radiofrequency ablation (*5–6*). However, there is still a lack of evidence-based medical guidelines regarding the treatment of patients with ultra-high HBV viral load, particularly those in the IT phase (*7*). Therefore, it is crucial to investigate the

clinical features of individuals with ultra-high HBV viral load and identify those at risk of developing HCC.

This study analyzed data from all patients with an HBV DNA level greater than 1×10^7 IU/mL at Peking University People's Hospital between January 2010 and March 2023. Demographic information, liver function parameters, and markers related to HBV infection were collected to investigate the clinical characteristics of individuals with an ultra-high HBV viral load, identify medium to high-risk populations for developing HCC, and provide new indications for antiviral treatment.

METHODS

This retrospective cross-sectional study was conducted at Peking University People's Hospital. Chronic HBV infection was defined as the persistent presence of serum HBsAg for more than 6 months. CHB patients meeting the following criteria were included in the study: HBsAg positive for >6 months; HBV DNA $>1\times10^7$ IU/mL; no prior or current antiviral treatment; no concomitant cirrhosis and HCC; and no missing data on HBeAg. Patients with other concurrent viral hepatitis or chronic liver diseases, including primary biliary cholangitis (PBC), autoimmune hepatitis (AIH), alcoholic liver disease (ALD), and nonalcoholic fatty liver disease (NAFLD), et al., were excluded from this study. The research protocol was approved by the Ethics Committee of Peking University People's Hospital (2023PHB053-001) and was conducted in accordance with the principles outlined in the 1975 Declaration of Helsinki and its 1983 revision.

HBV serological and virological markers including HBsAg, HBeAg, and HBV DNA levels were assessed. Liver function indexes include ALT, aspartate transaminase (AST), gamma-glutamyl transpeptidase (GGT), alkaline phosphatase (ALP), total bilirubin (TBIL), and albumin (ALB). Hematological index includes platelet (PLT) count. FIB-4 [Age (year) $\times$ AST (U/L) / (PLT ($\times10^9$/L) $\times$ ALT (U/L)$^{1/2}$] was calculated to evaluate the extent of liver fibrosis, whose score ≥3.25 could diagnose liver fibrosis and Metavir score $\geq$F3, while FIB-4 <1.45 could exclude Metavir score $\geq$F3. aMAP[({0.06 $\times$ age (year) + 0.89 $\times$ sex (Male: 1, Female: 0) + 0.48 [$\log_{10}$BIL (μmol/L) $\times$ 0.66 + (ALB (g/L) $\times$ –0.085)] – 0.01 $\times$ PLT (10^3/mm^3)} + 7.4) / 14.77 $\times$ 100] was calculated to predict HCC occurrence, whose score ≥50 indicates a medium to high risk of HCC.

The gold standard for staging chronic HBV infection relies on liver pathology; however, obtaining this in clinical practice is challenging. Therefore, in our study, we developed a new staging method based on HBeAg status, ALT level, and/or FIB-4 (eALT-F) to assess the risk of HCC in patients with an ultra-high viral HBV load.

The Kolmogorov-Smirnov test was utilized to assess the normality of the data. The baseline characteristics of the enrolled patients were described as follows: normally distributed data (e.g. age, HBV DNA, ALB, ALP, PLT, and aMAP) were presented as mean±standard deviation (SD), while non-normally distributed continuous data (e.g. HBsAg, HBeAg, ALT, AST, GGT, TBIL, and FIB-4) were reported as median [interquartile range (IQR)]. Categorical variables (e.g. gender, age grouping, ALT level grouping, FIB-4 grouping, and aMAP grouping) were presented as numbers (%). We used chi-square tests for categorical variables, Mann-Whitney tests for non-normally distributed continuous variables, and independent sample T tests for normally distributed continuous variables to detect significant differences between groups. All significance tests were two-tailed, with P-value <0.05 indicating statistical significance. Statistical analysis was performed using the R software package (http://www.R-project.org, version 4.1.1, R Foundation for Statistical Computing, Vienna, Austria).

RESULTS

Clinical Characteristics of Patients with Ultra-High HBV Viral Load

A total of 2,118 individuals with HBV DNA$>1\times10^7$ IU/mL detected for the first visit from January 2010 to March 2023 at Peking University People's Hospital were enrolled in this study. Patients meeting the following criteria were excluded: prior or current antiviral therapy (n=94); cirrhosis and HCC (n=51); missing data for HBeAg (n=425); and coexistence of hepatitis C virus (HCV), hepatitis D virus (HDV), or human immunodeficiency virus (HIV) (n=11); alcohol consumption >20 g/day (ALD) (n=7) and NAFLD (n=19). Finally, 1,511 CHB patients who had not undergone antiviral treatment with HBV DNA $>1\times10^7$ IU/mL have been enrolled in our study (Figure 1). The baseline features of CHB patients with
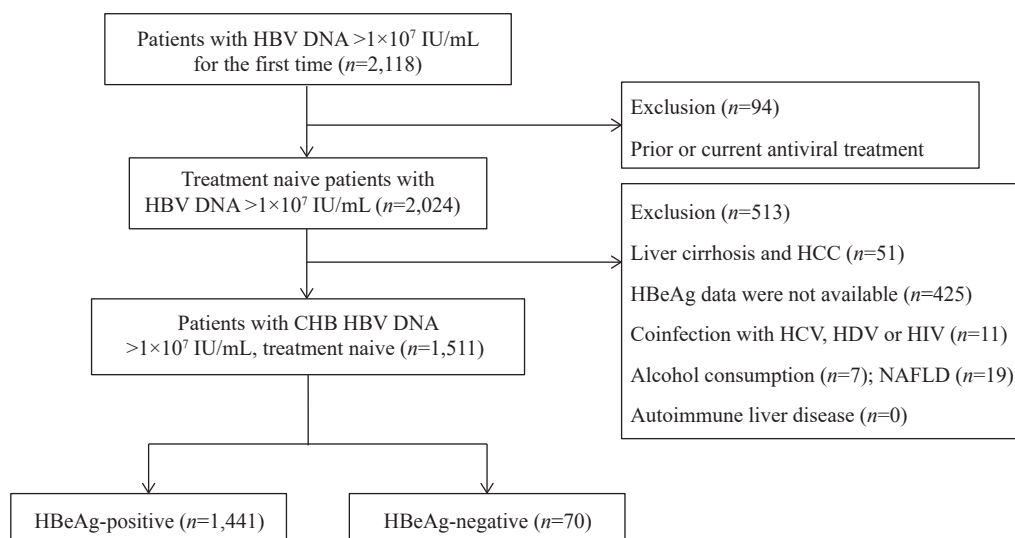
```
┌─────────────────────────────────────┐
│ Patients with HBV DNA >1×10⁷ IU/mL  │
│   for the first time (n=2,118)      │
└─────────────────────────────────────┘
```

$$\text{Patients with HBV DNA} >1\times10^7 \text{ IU/mL for the first time } (n=2{,}118)$$

Exclusion (n=94)

Prior or current antiviral treatment

$$\text{Treatment naive patients with HBV DNA} >1\times10^7 \text{ IU/mL } (n=2{,}024)$$

Exclusion (n=513)

Liver cirrhosis and HCC (n=51)

HBeAg data were not available (n=425)

Coinfection with HCV, HDV or HIV (n=11)

Alcohol consumption (n=7); NAFLD (n=19)

Autoimmune liver disease (n=0)

$$\text{Patients with CHB HBV DNA} >1\times10^7 \text{ IU/mL, treatment naive } (n=1{,}511)$$

HBeAg-positive (n=1,441)   HBeAg-negative (n=70)

FIGURE 1. The Flow chart of selecting patients with ultra-high HBV viral load.
Abbreviation: HBV=hepatitis B virus; CHB=chronic hepatitis B; HCC=hepatocellular carcinoma; HCV=hepatitis C virus; HDV=hepatitis D virus; HIV=human immunodeficiency virus; NAFLD=nonalcoholic fatty liver disease.

ultra-high HBV viral load are presented in Table 1. Except for younger patients, there were still a small proportion of older people (>60 years old) who showed ultra-high HBV viral load (4.3%). The median HBV DNA level was higher than 8.0 $\log_{10}$ IU/mL. Approximately, 2/3 of patients have ALT levels above the detection threshold (40 IU/L). There were 102 (9.1%) and 73 (6.7%) patients with FIB-4>3.25 and aMAP≥50, respectively.

Inadequacy of Traditional HBV Natural History Phases for Managing High-Risk HCC Populations

According to the status of HBeAg and ALT-level in the 2017 ESAL CHB guideline, 1,448 ultra-high HBV viral load patients were divided into four traditional phases: HBeAg positive-chronic infection, with positive HBeAg and ALT level<40 IU/L (n=528), HBeAg positive-chronic hepatitis, with positive HBeAg and ALT level >40 IU/L (n=833), HBeAg negative-chronic infection, with negative HBeAg and ALT level <40 IU/L (n=14) and HBeAg negative-chronic hepatitis, with negative HBeAg and ALT level >40 IU/L (n=73). Patients in the stage of HBeAg positive-chronic infection showed higher HBV DNA levels compared to the other groups (P<0.001). However, regardless of the phase, there is a certain proportion of patients at risk of developing HCC, even in the HBeAg negative-chronic infection phase (Table 2, Figure 2A). Therefore, this traditional staging method is not suitable for managing the HCC risk population.

Identifying HCC Risk in High HBV Load Patients via 'eALT-F' Staging

To better manage patients with ultra-high HBV viral load at risk of developing HCC, we endeavored to develop a novel staging method. By combining the 2016 American Association for the Study of Liver Diseases (AASLD) CHB guidelines with the aMAP score (8–9), a total of 1,092 patients were reclassified into four new phases, referred to as the 'eALT-F' stages: 1) HBeAg positive-chronic infection (n=142), characterized by positive HBeAg, normal ALT levels [the upper limit of normal (ULN) for ALT was 30 IU/L for males and 19 IU/L for females], and FIB-4 <1.45; 2) HBeAg positive-chronic hepatitis (n=869), characterized by positive HBeAg, elevated ALT levels, and/or FIB-4 ≥1.45; 3) HBeAg negative-chronic infection (n=4), characterized by negative HBeAg, normal ALT levels, and FIB-4 <1.45; and 4) HBeAg negative-chronic hepatitis (n=77), characterized by negative HBeAg, elevated ALT levels, and/or FIB-4 ≥ 1.45 (Table 3). According to the 'eALT-F' staging method, all patients at risk of HCC (aMAP score ≥50) were classified as having chronic hepatitis, regardless of HBeAg status (n=56 or 17, Figure 2B). In addition, individuals with an ultra-high viral HBV load who had ALT levels lower than 30 IU/L for males or 19 IU/L for females, and FIB4 <1.45, could be reliably identified as having no risk of developing HCC (aMAP

TABLE 1. Baseline characteristics of CHB patients with HBV DNA >1×10^7 IU/mL, treatment naive.

Index	Total (*n*=1,511)	HBeAg-positive (*n*=1,441)	HBeAg-negative (*n*=70)	*P*
Age (years)	34.6±11.5	34.2±11.3	44.1±11.0	<0.001
<30	606 (40.1)	602 (41.8)	4 (5.7)	<0.001
30–60	840 (55.6)	780 (54.1)	60 (85.7)	
≥60	65 (4.3)	59 (4.1)	6 (8.6)	
Male (%)	942 (62.3)	889 (61.7)	53 (75.7)	0.018
HBV DNA (log$_{10}$ IU/mL)	8.0±0.5	8.0±0.5	7.6±0.4	<0.001
HBsAg (COI)	34,132.8 (11,512.7, 61,309.7)	36,254.6 (13,788.6, 62,189.2)	5,537.1 (2,933.6, 9,656.2)	<0.001
HBeAg (COI)	1,376.2 (924.2, 1581.3)	1,399.1 (1,044.1, 1,591.7)	0.3 (0.3, 0.4)	<0.001
ALT (U/L)	85.0±35.8	84.5±35.9	94.8±32.2	<0.001
<40	542 (37.4)	532 (38.6)	10 (14.3)	<0.001
40–80	363 (25.1)	354 (25.7)	9 (12.9)	
≥80	543 (37.5)	492 (35.7)	51 (72.9)	
AST (U/L)	38.0 (24.0, 80.0)	36.0 (24.0, 74.0)	109.5 (59.5, 208.5)	<0.001
GGT (U/L)	27.0 (17.0, 50.0)	25.0 (16.0, 49.0)	45.5 (33.5, 86.0)	<0.001
ALP (U/L)	85.0±35.8	84.5±35.9	94.8±32.2	0.021
ALB (g/L)	44.5±4.2	44.6±4.0	42.8±6.1	<0.001
TBIL (μmol/L)	15.2 (11.8, 20.3)	15.0 (11.7, 20.2)	17.1 (13.1, 23.1)	0.002
PLT (×10^9/L)	211.1±62.3	212.8±61.5	184.1±69.5	<0.001
FIB-4	0.9 (0.6, 1.6)	0.8 (0.6, 1.5)	2.1 (1.2, 4.1)	<0.001
<1.45	803 (71.8)	779 (74)	24 (36.4)	<0.001
1.45–3.25	214 (19.1)	194 (18.4)	20 (30.3)	
>3.25	102 (9.1)	80 (7.6)	22 (33.3)	<0.001
aMAP	37.8±7.3	37.5±7.1	43.3±8.1	<0.001
<50	1,019 (93.3)	969 (94.4)	50 (76.9)	<0.001
≥50	73 (6.7)	58 (5.6)	15 (23.1)	

Abbreviation: CHB=chronic hepatitis B; HBV=hepatitis B virus; HBsAg=HBV surface antigen; HBeAg=HBV e antigen; ALT=alanine aminotransferase; AST=aspartate aminotransferase; GGT=gamma-glutamyl transpeptidase; ALP=alkaline phosphatase; ALB=Albumin; TBIL=total bilirubin; PLT=platelet count; FIB-4=Fibrosis 4 score.

score <50, *n*=142 or 4). The area under the receiver operating characteristic (AUROC) curve for the novel 'eALT-F' method was 0.977 (0.968–0.986), with a sensitivity of 0.959 (0.913–1.000), specificity of 0.910 (0.913–0.927), positive predictive value of 0.432 (0.356–0.508), and negative predictive value of 0.997 (0.993–1.000).

DISCUSSION

This study was based on HBV DNA >10^7 IU/mL as the threshold for ultra-high viral load according to the 2017 EASL CHB Guideline and the 2021 US hepatitis B Management Algorithm Update (*2*,*9*). Ultra-high viral load implies active HBV replication, strong infectivity, poor treatment response, and a certain relationship with the occurrence of end-stage liver diseases, including cirrhosis and HCC, et al (*10*). The conventional natural history staging for chronic HBV infection comprises four phases: IT, immune activation phase with positive HBeAg, low replication phase, and reactivation phase with negative HBeAg phases, with levels of HBV DNA >10^7 IU/mL, 10^4–10^7 IU/mL, <2,000 IU/mL, and >2,000 IU/mL, respectively (*9*). Based on this, HBV DNA >10^7 IU/mL should belong to the IT stage, and chronic HBV infection in the IT period is considered not to require active antiviral therapy due to the absence or mild inflammation of liver cells, slow progression of the disease, low risk of liver cirrhosis and HCC, and poor treatment response (*11*). However, there have been reports indicating a positive association between baseline HBV DNA levels and the risk of HCC, as well as the need for antiviral treatment in the IT phase (*12*).

TABLE 2. Clinical characteristics of patients in four traditional natural history stages of CHB.

Index	HBeAg-positive (n=1,361)		HBeAg-negative (n=87)		P
	Chronic infection (n=528)	Chronic hepatitis (n=833)	Chronic infection (n=14)	Chronic hepatitis (n=73)	
Age (years)	33.4±11.5	34.3±10.9	46.2±12.2	44.1±10.9	<0.001
<30	244 (46.2)	329 (39.5)	2 (14.3)	3 (4.1)	<0.001
30–60	261 (49.4)	472 (56.7)	10 (71.4)	64 (87.7)	
≥60	23 (4.4)	32 (3.8)	2 (14.3)	6 (8.2)	
Male (%)	245 (46.4)	598 (71.8)	11 (78.6)	53 (72.6)	<0.001
HBV DNA (log$_{10}$ IU/mL)	8.1±0.5	7.9±0.5	7.9±0.6	7.6±0.4	<0.001
HBsAg (COI)	54,200.7 (34,117.8, 77,197.1)	25,149.3 (9,330.6, 50,020.3)	3,034.8 (2,488.9, 6,499.4)	5,254.5 (2,589.5, 9,656.2)	<0.001
HBeAg (COI)	1,498.8 (1353.7, 1634.2)	1,273.4 (799.0, 1539.2)	0.3 (0.3, 0.4)	0.3 (0.3, 0.4)	<0.001
ALT (U/L)	25.0 (19.0, 31.0)	95.0 (58.0, 190.0)	30.0 (25.8, 35.8)	167.0 (99.0, 360.0)	<0.001
AST (U/L)	23.0 (20.0, 26.0)	60.0 (39.0, 110.0)	31.0 (21.2, 48.0)	120.0 (70.0, 218.0)	<0.001
GGT (U/L)	16.0 (13.0, 22.0)	38.0 (23.0, 68.0)	26.0 (22.0, 55.0)	46.0 (35.0, 76.0)	<0.001
ALP (U/L)	77.3±35.9	89.3±35.5	90.4±31.6	90.9±31.5	<0.001
ALB (g/L)	45.2±3.7	44.2±4.3	43.8±5.0	43.1±5.9	<0.001
TBIL (μmol/L)	13.6 (10.9, 17.7)	16.1 (12.4, 21.7)	14.3 (11.9, 24.8)	18.4 (13.3, 22.8)	<0.001
PLT (×10^9/L)	225.3±62.2	206.6±60.1	174.1±70.0	187.5±65.0	<0.001
FIB4	0.7 (0.5, 0.9)	1.0 (0.7, 1.8)	1.2 (0.9, 2.3)	2.1 (1.3, 4.0)	<0.001
<1.45	332 (88.8)	441 (66.5)	8 (66.7)	22 (31.4)	<0.001
1.45–3.25	32 (8.6)	156 (23.5)	1 (8.3)	25 (35.7)	
>3.25	10 (2.7)	66 (10)	3 (25)	23 (32.9)	
aMAP	35.6±6.9	38.4±6.9	44.5±9.5	42.9±7.4	<0.001
<50	354 (95.9)	601 (93.6)	9 (75)	55 (79.7)	<0.001
≥50	15 (4.1)	41 (6.4)	3 (25)	14 (20.3)	

Abbreviation: CHB=chronic hepatitis B; HBV=hepatitis B virus; HBsAg=HBV surface antigen; HBeAg=HBV e antigen; ALT=alanine aminotransferase; AST=aspartate aminotransferase; GGT=gamma-glutamyl transpeptidase; ALP=alkaline phosphatase; ALB=Albumin; TBIL=total bilirubin; PLT=platelet count; FIB-4=Fibrosis 4 score.

Previously, the traditional natural history phases have played a significant role in managing chronic HBV infection. However, as our understanding of HBV infection deepens and antiviral therapy develops, its limitations have become increasingly apparent: 1) Although it is based on immunological characteristics, there is no corresponding immunological evidence or indicators to define it. Some studies have even found that children and adolescent IT patients do not exhibit the immune tolerant T lymphocyte characteristics (13). 2) The current staging cannot include all chronic HBV carriers, leading to several 'gray areas' (14). 3) The value of guiding treatment and predicting prognosis is decreasing, and with the emergence of new anti-HBV drugs and the expansion of anti-HBV indications, this value will further decrease (9). Professor Zhuang mentioned that a considerable number of patients in the 'IT period' have obvious liver cell inflammation, necrosis, and pathological changes of liver fibrosis (15).

In this case, these patients should not be categorized into the IT period and should not be treated as 'gray areas'. They should be classified as CHB with positive or negative HBeAg.

As current treatment strategies for chronic HBV infection focus on 'treat more' as opposed to 'treat all,' it is recommended that only HBeAg status, degree of liver inflammation, and non-invasive liver fibrosis scores be employed as the basis for staging chronic HBV-infected patients. The commonly used substitute indicator for liver inflammation in clinical practice is ALT. A study showed that even according to the AASLD regulation of 35 IU/mL for men and 25 IU/mL for women, 28.7% of HBV-infected individuals without significant fibrosis and with normal ALT still have significant inflammation (16). Therefore, the ULN of the new staging method for ALT was selected from the relatively recognized domestic and international 30 IU/mL for males and 19
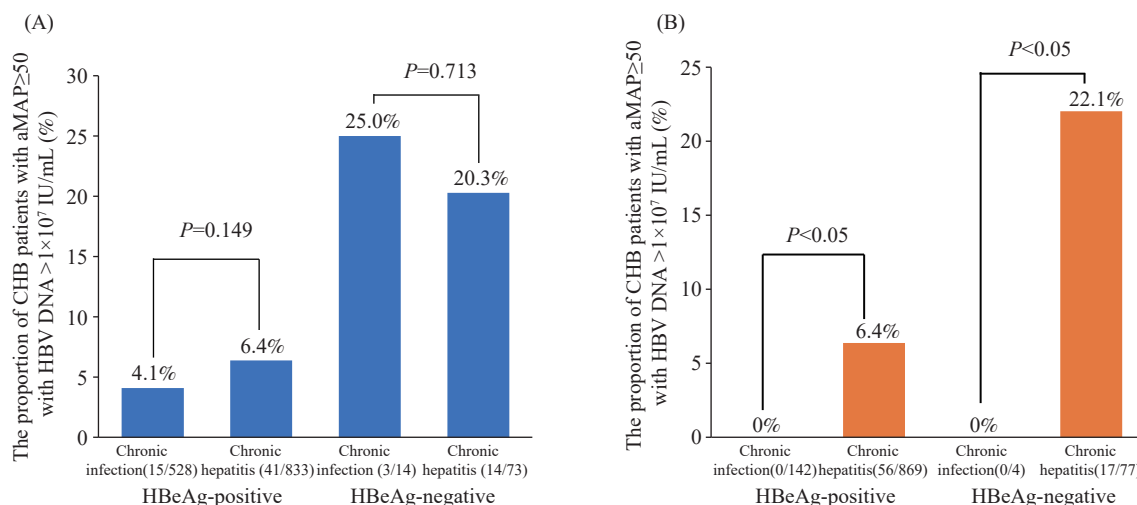
FIGURE 2. The proportion of CHB patients with aMAP≥50 in (A) traditional natural history stages and (B) 'eALT-F' stages of CHB.
Notes: in panel A, significant differences in the proportion of aMAP≥50 was not observed among the patients in four traditional natural history stages of CHB; In panel B, significant differences in the proportion of aMAP≥50 was observed among the patients in four 'eALT-F' stages of CHB.
Abbreviation: CHB=chronic hepatitis B; HBeAg=HBV e antigen; HBV=Hepatitis B virus.

IU/mL for females (*17*). There are various non-invasive alternative indicators for liver fibrosis, among which FIB-4 is easy to use and widely recognized for its evaluation efficacy (*18*). FIB-4, in addition to evaluating the degree of liver fibrosis, is also useful in predicting HCC risk and even liver disease-related death (*19*). Kim et al. retrospectively analyzed 413 cases of HBV infection during the IT phase, and stratification analysis revealed that patients with FIB-4 >1.45 had a significantly higher 5-year cumulative incidence of HCC compared to those with FIB-4 <1.45 (*20*). Following 'eALT-F,' the new staging method, in our study, those with HBeAg-positive chronic infection and chronic hepatitis account for 13.0% and 79.6%, respectively, and those with HBeAg-negative chronic infection and chronic hepatitis account for 0.4% and 7.0%, respectively.

The objective of CHB treatment is to minimize the occurrence of end-stage liver disease, particularly HCC, which is a slow process. To achieve this, we utilized the widely recommended HCC risk score-aMAP to assess the risk of HCC in individuals infected with chronic HBV and guide the selection of antiviral treatment indications (*11*). The aMAP score, which was developed and externally validated by Chinese pathologists and their collaborators, encompasses age, male gender, albumin, bilirubin, and platelet data. An aMAP score of ≥50 indicates a medium to high risk of HCC. A recent study demonstrated that the aMAP

score has substantial value in evaluating advanced liver fibrosis and cirrhosis in patients with CHB (*21*). Our study reveals that according to the 2017 EASL guideline, among individuals with ultra-high HBV viral load and an aMAP score of ≥50, 24.7% (18/73) of patients in both HBeAg-positive and -negative chronic infected stages do not require antiviral treatment. This suggests that these patients, who should receive antiviral treatment, have not been treated. According to the new 'eALT-F' staging method, the aMAP scores in all HBeAg-positive and -negative chronic carriers with ultra-high viral load were lower than 50. This indicates that the new staging effectively excludes and identifies medium-high risk patients with HCC occurrence.

In summary, patients with CHB who have an ultra-high viral load, elevated ALT levels (the ALT was 30 IU/L for males and 19 IU/L for females), and/or FIB-4 ≥1.45 should receive active antiviral treatment. For individuals with simple chronic infection and normal ALT levels and FIB-4 <1.45, further observation can be conducted and evaluated every six months. Once the values go beyond this range, timely antiviral treatment should be initiated. The decision to initiate antiviral treatment for HBV-infected individuals with an ultra-high viral load is not only based on indications, but also on the risk of HCC, specifically the aMAP score and its changing trend.

Conflicts of interest: No conflicts of interest.

TABLE 3. Clinical characteristics of patients in four 'eALT-F' stages of CHB.

Index	HBeAg-positive (n=1,011)		HBeAg-negative (n=81)		P
	Chronic infection (n=142)	Chronic hepatitis (n=869)	Chronic infection (n=4)	Chronic hepatitis (n=77)	
Age (years)	31.9±7.9	35.7±11.6	40.2±12.1	44.4±11.3	<0.001
<30	63 (44.4)	307 (35.3)	1 (25)	4 (5.2)	<0.001
30–60	79 (55.6)	516 (59.4)	3 (75)	65 (84.4)	
≥60	0 (0)	46 (5.3)	0 (0)	8 (10.4)	
Male (%)	83 (58.5)	543 (62.5)	3 (75)	56 (72.7)	0.179
HBV DNA (log$_{10}$ IU/mL)	8.1±0.5	8.0±0.5	7.6±0.5	7.7±0.5	<0.001
HBsAg (COI)	59,710.6 (40,016.6, 80,457.6)	28,824.2 (10,367.2, 55,875.4)	2,679.6 (2,634.8, 4,125.7)	5,297.2 (2,712.3, 10,018.8)	<0.001
HBeAg (COI)	1,544.0 (1,411.3, 1,682.9)	1,340.3 (881.2, 1,565.0)	0.3 (0.3, 0.4)	0.3 (0.3, 0.4)	<0.001
ALT (U/L)	19.0 (15.0, 24.0)	70.0 (38.0, 155.0)	24.5 (20.0, 28.0)	136.0 (77.0, 331.0)	<0.001
AST (U/L)	21.0 (18.0, 23.0)	46.0 (28.0, 92.0)	21.0 (19.2, 24.2)	115.0 (64.0, 218.0)	<0.001
GGT (U/L)	16.0 (13.0, 21.0)	30.0 (19.5, 57.0)	29.5 (23.8, 36.0)	46.0 (33.0, 85.0)	<0.001
ALP (U/L)	78.8±29.2	86.3±34.1	85.0±11.2	92.2±32.4	0.029
Albumin (g/L)	45.9±3.2	44.1±4.4	45.4±2.9	43.0±5.9	<0.001
TBIL (μmol/L)	14.4 (11.0, 18.6)	15.4 (12.0, 20.8)	13.1 (11.4, 22.3)	17.9 (13.1, 22.5)	0.002
PLT (×10^9/L)	233.3±51.5	209.6±62.7	222.0±79.7	183.3±65.1	<0.001
FIB4	0.7 (0.5, 0.8)	0.9 (0.6, 1.7)	1.0 (0.8, 1.1)	2.1 (1.3, 4.0)	<0.001
<1.45	142 (100)	608 (70)	4 (100)	26 (33.8)	<0.001
1.45–3.25	0 (0)	185 (21.3)	0 (0)	25 (32.5)	
>3.25	0 (0)	76 (8.7)	0 (0)	26 (33.8)	
aMAP	34.5±5.1	37.9±7.2	39.1±6.0	43.3±7.8	<0.001
<50	142 (100)	813 (93.6)	4 (100)	60 (77.9)	<0.001
≥50	0 (0)	56 (6.4)	0 (0)	17 (22.1)	

Abbreviation: CHB=chronic hepatitis B; HBV=hepatitis B virus; HBsAg=HBV surface antigen; HBeAg=HBV e antigen; ALT=alanine aminotransferase; AST=aspartate aminotransferase; GGT=gamma-glutamyl transpeptidase; ALP=alkaline phosphatase; ALB=Albumin; TBIL=total bilirubin; PLT=platelet count; FIB-4=Fibrosis 4 score.

Corresponding authors: Bo Feng, fengbo@pkuph.edu.cn; Xiaoxiao Wang, wangxx0635@163.com.

¹ Peking University People's Hospital, Peking University Hepatology Institute, Beijing, China; ² Peking University People's Hospital, Peking University Hepatology Institute, Beijing Key Laboratory of Hepatitis C and Immunotherapy for Liver Diseases, Beijing International Cooperation Base for Science and Technology on NAFLD Diagnosis, Beijing, China.
& Joint first authors.

REFERENCES

1. Chinese Society of Hepatology, Chinese Medical Association, Chinese Society of Infectious Diseases, Chinese Medical Association. Guidelines for the prevention and treatment of chronic hepatitis B (Version 2022). Chin J Infect Dis 2022;30(12):1309 – 31. http://dx.doi.org/10.3760/cma.j.cn501113-20221204-00607. (In Chinese).
2. Martin P, Nguyen MH, Dieterich DT, Lau DTY, Janssen HLA, Peters MG, et al. Treatment algorithm for managing chronic hepatitis b virus infection in the united states: 2021 update. Clin Gastroenterol Hepatol 2022;20(8):1766 – 75. http://dx.doi.org/10.1016/j.cgh.2021.07.036.
3. Nguyen VTT, Law MG, Dore GJ. Hepatitis B-related hepatocellular carcinoma: epidemiological characteristics and disease burden. J Viral Hepat 2009;16(7):453 – 63. http://dx.doi.org/10.1111/j.1365-2893.2009.01117.x.
4. Chen CJ, Yang HI, Su J, Jen CL, You SL, Lu SN, et al. Risk of hepatocellular carcinoma across a biological gradient of serum hepatitis B virus DNA level. JAMA 2006;295(1):65 – 73. http://dx.doi.org/10.1001/jama.295.1.65.
5. Meng C, Liu T, Liu YW, Zhang LZ, Wang YL. Hepatitis B virus cccdna in hepatocellular carcinoma tissue increases the risk of recurrence after liver transplantation. Transplant Proc 2019;51(10):3364 – 8. http://dx.doi.org/10.1016/j.transproceed.2019.04.020.
6. Yang Y, Wen F, Li JL, Zhang PF, Yan WH, Hao P, et al. A high

baseline HBV load and antiviral therapy affect the survival of patients with advanced HBV-related HCC treated with sorafenib. Liver Int 2015;35(9):2147 – 54. http://dx.doi.org/10.1111/liv.12805.

7. Klair JS, Vancura J, Murali AR. PRO: Patients with chronic hepatitis B in immune-tolerant phase should be treated. Clin Liver Dis (Hoboken) 2020;15(1):21 – 4. http://dx.doi.org/10.1002/cld.892.

8. Fan R, Papatheodoridis G, Sun J, Innes H, Toyoda H, Xie Q, et al. aMAP risk score predicts hepatocellular carcinoma development in patients with chronic hepatitis. J Hepatol 2020;73(6):1368 – 78. http://dx.doi.org/10.1016/j.jhep.2020.07.025.

9. European Association for the Study of the Liver. EASL 2017 clinical practice guidelines on the management of hepatitis B virus infection. J Hepatol 2017;67(2):370 – 98. http://dx.doi.org/10.1016/j.jhep.2017.03.021.

10. Stella L, Santopaolo F, Gasbarrini A, Pompili M, Ponziani FR. Viral hepatitis and hepatocellular carcinoma: from molecular pathways to the role of clinical surveillance and antiviral treatment. World J Gastroenterol 2022;28(21):2251 – 81. http://dx.doi.org/10.3748/wjg.v28.i21.2251.

11. Liaw YF. Perspectives on current controversial issues in the management of chronic HBV infection. J Gastroenterol 2022;57(11):828 – 37. http://dx.doi.org/10.1007/s00535-022-01918-z.

12. Hong YM, Yoon KT. Definition and management of the immune tolerance phase in chronic hepatitis B. Korean J Gastroenterol 2022;79(4):156 – 60. http://dx.doi.org/10.4166/kjg.2022.049.

13. Kennedy PTF, Sandalova E, Jo J, Gill U, Ushiro-Lumb I, Tan AT, et al. Preserved T-cell function in children and young adults with immune-tolerant chronic hepatitis B. Gastroenterology 2012;143(3):637 – 45. http://dx.doi.org/10.1053/j.gastro.2012.06.009.

14. Huang DQ, Li XH, Le MH, Le AK, Yeo YH, Trinh HN, et al. Natural history and hepatocellular carcinoma risk in untreated chronic hepatitis B patients with indeterminate phase. Clin Gastroenterol Hepatol 2022;20(8):1803 – 12.e5. http://dx.doi.org/10.1016/j.cgh.2021.01.019.

15. Zhuang H. Should patients in the immune tolerance stage of chronic hepatitis B virus infection be treated? J Clin Hepatol 2021;37(2):272-7. http://dx.doi.org/10.3969/j.issn.1001-5256.2021.02.007. (In Chinese).

16. Liu JC, Wang J, Yan XM, Xue RF, Zhan J, Jiang SL, et al. Presence of liver inflammation in asian patients with chronic hepatitis B with normal ALT and detectable HBV DNA in absence of liver fibrosis. Hepatol Commun 2022;6(4):855 – 66. http://dx.doi.org/10.1002/hep4.1859.

17. Newsome PN, Cramb R, Davison SM, Dillon JF, Foulerton M, Godfrey EM, et al. Guidelines on the management of abnormal liver blood tests. Gut 2018;67(1):6 – 19. http://dx.doi.org/10.1136/gutjnl-2017-314924.

18. Kaya A, Barutcu S, Gülsen MT. Evaluation of fibrosis with noninvasive biochemical tests in chronic viral hepatitis B. Hepatol Forum 2023;4(1):25 – 9. http://dx.doi.org/10.14744/hf.2022.2022.0025.

19. Tseng TC, Choi J, Nguyen MH, Peng CY, Siakavellas S, Papatheodoridis G, et al. One-year fibrosis-4 index helps identify minimal HCC risk in non-cirrhotic chronic hepatitis B patients with antiviral treatment. Hepatol Int 2021;15(1):105 – 13. http://dx.doi.org/10.1007/s12072-020-10124-z.

20. Kim GA, Lim YS, Han S, Choi J, Shim JH, Kim KM, et al. High risk of hepatocellular carcinoma and death in patients with immune-tolerant-phase chronic hepatitis B. Gut 2018;67(5):945 – 52. http://dx.doi.org/10.1136/gutjnl-2017-314904.

21. Fan R, Li GL, Yu N, Chang XJ, Arshad T, Liu WY, et al. Amap score and its combination with liver stiffness measurement accurately assess liver fibrosis in chronic hepatitis B patients. Clin Gastroenterol Hepatol 2023;21(12):3070 – 9.e13. http://dx.doi.org/10.1016/j.cgh.2023.03.005.

Indexed by Science Citation Index Expanded (SCIE), Social Sciences Citation Index (SSCI), PubMed Central (PMC), Scopus, Chinese Scientific and Technical Papers and Citations, and Chinese Science Citation Database (CSCD)